



# The Molecular Clouds in a Section of the Third Galactic Quadrant: Observational Properties and Chemical Abundance Ratio between CO and its Isotopologues

Chen Wang<sup>1,2,3</sup> , Haoran Feng<sup>2,3,4</sup> , Ji Yang<sup>2,3</sup> , Xuepeng Chen<sup>2,3</sup> , Yang Su<sup>2,3</sup> , Qing-Zeng Yan<sup>2,3</sup> , Fujun Du<sup>2,3,4</sup> , Yuehui Ma<sup>2,3</sup> , and Jiajun Cai<sup>5</sup>

<sup>1</sup> National Astronomical Observatories, Chinese Academy of Sciences, 20A Datun Road, Chaoyang District, Beijing 100101, People's Republic of China

<sup>2</sup> Purple Mountain Observatory, Chinese Academy of Sciences, 10 Yuanhua Road, Qixia District, Nanjing 210033, People's Republic of China; [jijiang@pmo.ac.cn](mailto:jijiang@pmo.ac.cn)

<sup>3</sup> Key Laboratory of Radio Astronomy and Technology, Chinese Academy of Sciences, A20 Datun Road, Chaoyang District, Beijing 100101, People's Republic of China

<sup>4</sup> University of Science and Technology of China, Chinese Academy of Sciences, Hefei 230026, People's Republic of China

<sup>5</sup> College of Science & Center for Astronomy and Space Sciences, China Three Gorges University, Yichang 443002, People's Republic of China

Received 2023 May 8; revised 2023 July 27; accepted 2023 July 30; published 2023 August 22

## Abstract

We compare the observational properties between  $^{12}\text{CO}$ ,  $^{13}\text{CO}$ , and  $\text{C}^{18}\text{O}$  and summarize the observational parameters based on a 7069-cloud sample from the Milky Way Imaging Scroll Painting CO survey in a section of the third Galactic quadrant. We find that the  $^{13}\text{CO}$  angular area ( $A_{^{13}\text{CO}}$ ) generally increases with that of  $^{12}\text{CO}$  ( $A_{^{12}\text{CO}}$ ), and the ratio of  $A_{^{13}\text{CO}}$  to  $A_{^{12}\text{CO}}$  is 0.38 by linear fitting. We find that the  $^{12}\text{CO}$  and  $^{13}\text{CO}$  flux are tightly correlated as  $F_{^{13}\text{CO}} = 0.17 F_{^{12}\text{CO}}$  with both fluxes calculated within the  $^{13}\text{CO}$ -bright region. This indicates that the abundance  $X_{^{13}\text{CO}}$  is a constant as  $6.5_{-0.5}^{+0.1} \times 10^{-7}$  for all samples under the assumption of local thermodynamic equilibrium (LTE). Additionally, we observed that the X-factor is approximately constant in a large sample of molecular clouds. Similarly, we find  $F_{\text{C}^{18}\text{O}} = 0.11 F_{^{13}\text{CO}}$  with both fluxes calculated within the  $\text{C}^{18}\text{O}$ -bright region, which indicates that the abundance ratio  $X_{^{13}\text{CO}}/X_{\text{C}^{18}\text{O}}$  stays at the same value of  $9.7_{-0.8}^{+0.6}$  across the molecular clouds under the LTE assumption. The linear relationships of  $F_{^{13}\text{CO}}$  versus  $F_{^{12}\text{CO}}$  and  $F_{^{13}\text{CO}}$  versus  $F_{\text{C}^{18}\text{O}}$  hold not only for the  $^{13}\text{CO}$ -bright region and  $\text{C}^{18}\text{O}$ -bright region, but also for the entire molecular cloud scale with a lower flux ratio. The abundance ratio  $X_{^{13}\text{CO}}/X_{\text{C}^{18}\text{O}}$  inside the clouds shows a strong correlation with the column density and temperature. This indicates that the ratio  $X_{^{13}\text{CO}}/X_{\text{C}^{18}\text{O}}$  is dominated by a combination of chemical fractionation, selective dissociation, and the self-shielding effect inside the clouds.

*Unified Astronomy Thesaurus concepts:* [Molecular clouds \(1072\)](#); [Chemical abundances \(224\)](#); [Abundance ratios \(11\)](#)

## 1. Introduction

Molecular clouds (MCs; Dame et al. 2001) are an important component of the interstellar medium (ISM) and serve as the birthplaces of stars. CO and its isotopologues,  $^{13}\text{CO}$  and  $\text{C}^{18}\text{O}$  ( $J = 1-0$ ), are effective tracers of MCs, providing valuable physical and chemical information under the assumption of local thermodynamic equilibrium (LTE; Pineda et al. 2008, 2010; Wilson et al. 2009). In general, the column density of molecular hydrogen can be estimated from their abundance (Nagahama et al. 1998; Rohlfs & Wilson 2000), with  $N(\text{H}_2)/N(^{13}\text{CO}) = 7 \times 10^5$  and  $N(\text{H}_2)/N(\text{C}^{18}\text{O}) = 7 \times 10^6$ . However, is the abundance of these tracers the same in all MCs? Or does their abundance systematically change during the evolution of MCs?

These questions have garnered significant attention in recent decades, and observational and theoretical efforts have been made to address them. van Dishoeck & Black (1988) demonstrated that the isotopic chemistry of CO is influenced by different physical processes and chemical reactions in various regions. For instance, CO rare isotopologues associated with OB stars or HII regions are selectively dissociated by far-ultraviolet (FUV) emission more effectively than CO due to differences in self-shielding effects (van Dishoeck & Black 1988;

Warin et al. 1996; Liszt 2007; Visser et al. 2009; Shimajiri et al. 2014, 2015).

On the other hand, the abundance ratio of CO isotopologues in dark clouds or cold cores is close to the terrestrial value (Wilson & Matteucci 1992), as these clouds lack FUV emission and have lower temperatures. This suggests that there are at least two types of MCs with different CO isotopic abundance ratios. In fact, case studies of MCs and simulation studies have confirmed this. The impacts of selective photodissociation and chemical fractionation of CO on the  $X_{^{12}\text{CO}}/X_{^{13}\text{CO}}$  isotopic ratio have been examined by Szűcs et al. (2014), and they found a close correlation between the ratio and both the  $^{12}\text{CO}$  and  $^{13}\text{CO}$  column densities.

In observational case studies, Wilson & Matteucci (1992) show a gradient in the  $^{12}\text{C}/^{13}\text{C}$  and  $^{16}\text{O}/^{18}\text{O}$  ratios with galactocentric distance, and get the terrestrial  $X_{^{13}\text{CO}}/X_{\text{C}^{18}\text{O}}$  value as 5.5. Furthermore, Wu et al. (2012) found that the mean abundance ratio of  $X_{^{13}\text{CO}}/X_{\text{C}^{18}\text{O}}$  in 674 Planck cold clumps from the Early Cold Core (ECC) catalog is 7 with the LTE assumption, based on a survey of the  $J = 1-0$  transitions of  $^{12}\text{CO}$ ,  $^{13}\text{CO}$ , and  $\text{C}^{18}\text{O}$  using the Purple Mountain Observatory (PMO) 13.7 m telescope. In the last decade, the effects of selective photodissociation have received more attention and discussion. Shimajiri et al. (2014) found that the mean  $X_{^{13}\text{CO}}/X_{\text{C}^{18}\text{O}}$  ratio in nearly edge-on photon-dominated regions is 16.47, which is much larger than the terrestrial value of 5.5 (Wilson & Matteucci 1992), while the  $X_{^{13}\text{CO}}/X_{\text{C}^{18}\text{O}}$  ratio in other regions was found to be 12.29, using the Nobeyama 45 m telescope in the  $J = 1-0$  transitions of CO isotopologues with the LTE assumption. Additionally,



Original content from this work may be used under the terms of the [Creative Commons Attribution 4.0 licence](#). Any further distribution of this work must maintain attribution to the author(s) and the title of the work, journal citation and DOI.

Kong et al. (2015) found significant spatial variations in the abundances of  $^{13}\text{CO}$  and  $\text{C}^{18}\text{O}$  in the southeastern part of the California MC that are correlated with the variations in gas temperature surveyed in the  $^{12}\text{CO}$ ,  $^{13}\text{CO}$ , and  $\text{C}^{18}\text{O}(J=2-1)$  with standard LTE analysis. Roueff et al. (2021) found that chemical effects play a significant role, by enhancing the  $^{13}\text{CO}$  abundance (fractionation) or destroying  $\text{C}^{18}\text{O}$  (photodissociation) when the  $X_{^{13}\text{CO}}/X_{\text{C}^{18}\text{O}}$  upper bound is close to 50 in the Orion B MC, using the Cramér–Rao bound (CRB) technique. These results indicate that  $X_{^{13}\text{CO}}/X_{\text{C}^{18}\text{O}}$  will change significantly with the presence of heating sources inside MCs. Importantly, our previous work, based on large-scale ( $58.5 \text{ deg}^2$ ) observations of  $^{12}\text{CO}$ ,  $^{13}\text{CO}$ , and  $\text{C}^{18}\text{O}$  ( $1-0$ ) transitions with the LTE assumption toward the Gemini OB1 MC Complex, found that clouds can be divided into two types based on  $X_{^{13}\text{CO}}/X_{\text{C}^{18}\text{O}}$  ratios (Wang et al. 2019). These two types of clouds exhibit systematic differences in their physical properties, such as excitation temperature and column density.

Although differences in isotopic abundance between MCs have been observed, it is not known whether these differences are systematic, due to the limited number of samples studied, and the exact physical explanation behind them remains unclear. Studying isotopic abundance in large samples can provide a way to address this problem.

The data in this study cover an area of  $250 \text{ deg}^2$  located in the third quadrant of the Milky Way. This paper is the third in a series of studies on large samples of MCs in this region. In Paper I (Wang et al. 2023), the data were described in detail, and 7069 clouds were identified based on the DBSCAN algorithm in the  $^{12}\text{CO}$  data. Additionally, we identified 1197 clouds with  $^{13}\text{CO}$  emission and 32 clouds with  $\text{C}^{18}\text{O}$  emission based on the stacking bump algorithm in the catalog of 7069 clouds. In Paper II (Ma et al. 2022), column density maps were obtained for an unbiased sample of 120 MCs in the data, and a relation between the dispersion of the normalized column density and the sonic Mach number of MCs was found, based on the same data and catalog.

In this paper, we study the fundamental properties of MCs, following the catalog in Paper I. The observations and data reduction are described in Section 2. In Section 3, we present the interesting results, which include a statistical study of the observational properties of MCs, optical depth, and flux results. The results of the abundance  $X_{^{13}\text{CO}}$  and abundance ratio  $X_{^{13}\text{CO}}/X_{\text{C}^{18}\text{O}}$  are presented in Sections 4 and 5, respectively. We will discuss some important issues in Section 6, and the conclusion is given in Section 7.

## 2. Data and Catalog

The data of the  $J=1-0$  transitions of  $^{12}\text{CO}$ ,  $^{13}\text{CO}$ , and  $\text{C}^{18}\text{O}$  were obtained with the PMO 13.7 m millimeter telescope (Yang et al. 2008; Shan et al. 2012). The data cover a section in the third Galactic quadrant ( $195^\circ < l < 220^\circ$ ,  $|b| < 5^\circ$ ) and are part of the Milky Way Imaging Scroll Painting (MWISP) project, which is a multiline Galactic plane survey in CO and its isotopic transitions. The mean noise  $\sigma$  is  $\sim 0.45 \text{ K}$  for  $^{12}\text{CO}$  with  $0.16 \text{ km s}^{-1}$  velocity resolution and  $\sim 0.25 \text{ K}$  for  $^{13}\text{CO}$  and  $\text{C}^{18}\text{O}$  with  $0.17 \text{ km s}^{-1}$  velocity resolution (Wang et al. 2023).

Paper I has described the data in detail and shown that 7069 clouds were identified based on the DBSCAN algorithm in the  $^{12}\text{CO}$  data<sup>6</sup>. We have also identified 1197 clouds with  $^{13}\text{CO}$  emission and 32 clouds with  $\text{C}^{18}\text{O}$  emission, based on the

stacking bump algorithm in the 7069-cloud catalog, respectively. In this paper, we study the fundamental properties of MCs following the catalog in Paper I.

## 3. Observational Properties between $^{12}\text{CO}$ , $^{13}\text{CO}$ , and $\text{C}^{18}\text{O}$

### 3.1. Peak Intensity

Observationally, the specific form of the radiative equation in the low-temperature approximation (Bourke et al. 1997) is given by

$$T_{\text{mb}} = \eta[J(T_{\text{ex}}) - J(T_{\text{bg}})](1 - \exp(-\tau)), \quad (1)$$

where  $T_{\text{mb}}$  is the observed brightness temperature,  $\eta$  is the beam filling factor (assumed to be 1, as discussed in Section 6.2), and  $J(T)$  is a function of temperature  $T$ , given by  $J(T) = h\nu/k \times (\exp(h\nu/kT) - 1)^{-1}$ .  $T_{\text{ex}}$  is the excitation temperature,  $T_{\text{bg}}$  is the background temperature, and  $\tau$  is the optical depth.

Assuming the MCs are in the LTE condition, we can obtain the excitation temperature using the  $^{12}\text{CO}$  ( $J=1-0$ ) emission line, which is generally known to be optically thick (e.g., Section 3.2). The calculation is based on the following formula (Nagahama et al. 1998; Rohlfs & Wilson 2000):

$$T_{\text{ex}} = \frac{5.53}{\ln\left(1 + \frac{5.53 \text{ K}}{T_{\text{mb}}(^{12}\text{CO}) + 0.819 \text{ K}}\right)} \text{ K}. \quad (2)$$

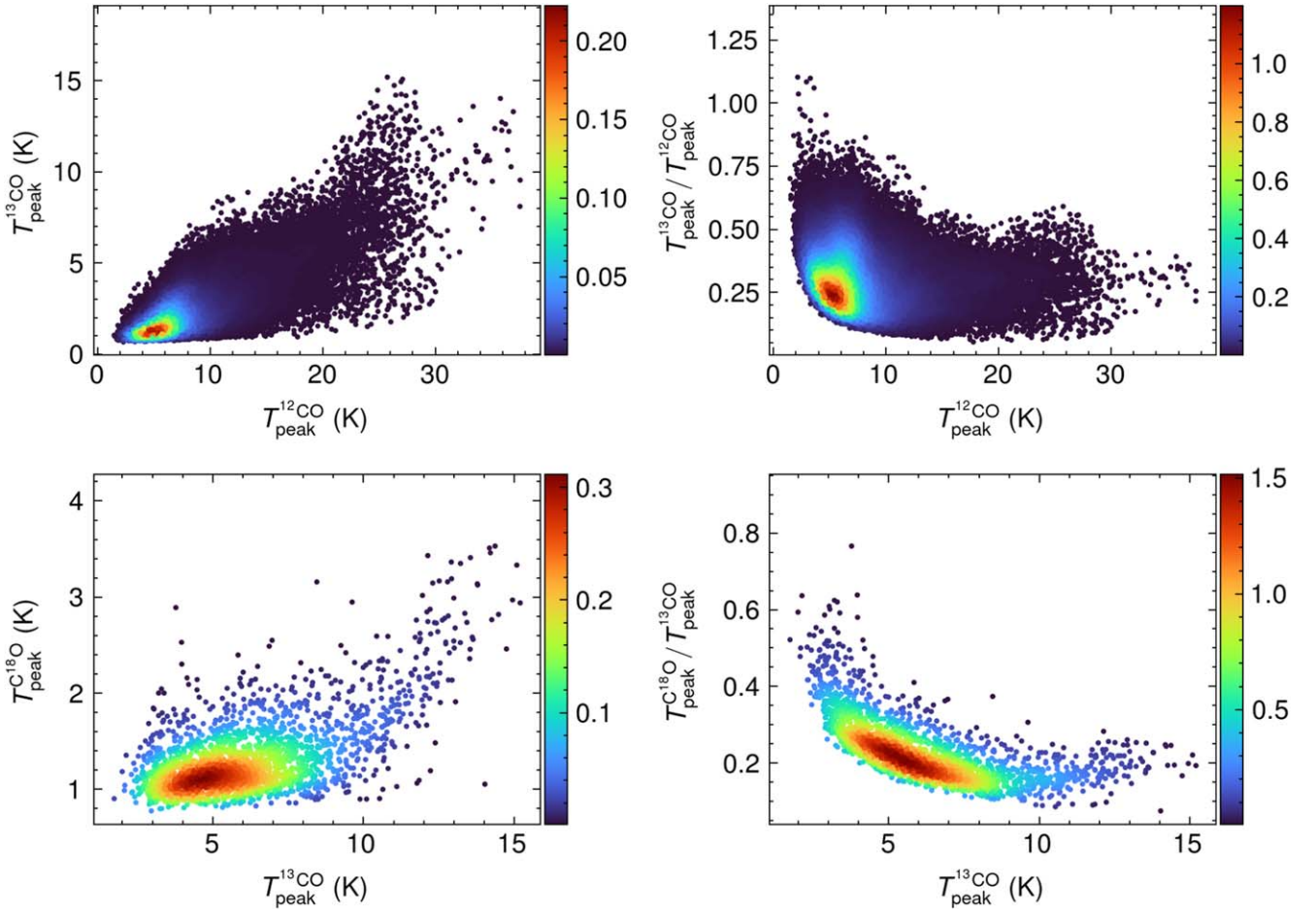
In order to avoid the influence of noise, we selected pixels based on the signal-to-noise ratio (S/N) for our statistical research. All of the pixels are from the cloud catalog described in Paper I. We considered only pixels with a spectral maximum greater than  $4\sigma$  ( $\sim 1.8 \text{ K}$  for  $^{12}\text{CO}$  and  $\sim 1 \text{ K}$  for  $^{13}\text{CO}$  and  $\text{C}^{18}\text{O}$ ). Additionally, we considered only velocity-integrated intensity pixels with an intensity greater than five times the intensity noise threshold ( $\sigma_i = \sigma\sqrt{N_{\text{channels}}}\Delta v_i$ , where  $N_{\text{channels}}$  is the number of channels in the spectrum).

Figure 1 shows  $T_{\text{peak}}^{^{13}\text{CO}}$  versus  $T_{\text{peak}}^{^{12}\text{CO}}$  measured pixel by pixel in 1197 clouds that have  $^{13}\text{CO}$  emission. The maximum  $T_{\text{peak}}^{^{12}\text{CO}}$  and  $T_{\text{peak}}^{^{13}\text{CO}}$  are 37.5 K and 15.2 K, respectively (Table 1). 88.3% of the pixels have  $T_{\text{peak}}^{^{13}\text{CO}}$  and  $T_{\text{peak}}^{^{12}\text{CO}}$  in the range of [1, 5] K and [1, 10] K, respectively.

Figure 1 presents  $T_{\text{peak}}^{^{13}\text{CO}}/T_{\text{peak}}^{^{12}\text{CO}}$  against  $T_{\text{peak}}^{^{12}\text{CO}}$  measured pixel by pixel in 1197 clouds that have  $^{13}\text{CO}$  emission. The dispersion of the peak ratio  $T_{\text{peak}}^{^{13}\text{CO}}/T_{\text{peak}}^{^{12}\text{CO}}$  decreases with  $T_{\text{peak}}^{^{12}\text{CO}}$ , and there is a bump distribution in the range of [20, 30] K.

The relationship between  $T_{\text{peak}}^{^{13}\text{CO}}$  and  $T_{\text{peak}}^{\text{C}^{18}\text{O}}$  in a catalog of 32 clouds that have  $\text{C}^{18}\text{O}$  emission is shown in Figure 1. The maximum  $T_{\text{peak}}^{\text{C}^{18}\text{O}}$  is 3.53 K. 81% of the pixels have  $T_{\text{peak}}^{\text{C}^{18}\text{O}}$  in the range of [0.7, 1.5] K. This shows that with limited sensitivity truncation, the S/Ns of  $^{12}\text{CO}$ ,  $^{13}\text{CO}$ , and  $\text{C}^{18}\text{O}$  obviously decrease sequentially. In the statistical analysis of  $\text{C}^{18}\text{O}$ , the selection effect caused by the detection sensitivity should be carefully considered. Similar to the distribution of  $T_{\text{peak}}^{^{13}\text{CO}}/T_{\text{peak}}^{^{12}\text{CO}}$ , Figure 1 shows that the ratio  $T_{\text{peak}}^{\text{C}^{18}\text{O}}/T_{\text{peak}}^{^{13}\text{CO}}$  decreases with  $T_{\text{peak}}^{^{13}\text{CO}}$  and stays in the range of [0.1, 0.3] in the high-value region of  $T_{\text{peak}}^{^{13}\text{CO}}$ .

<sup>6</sup> <https://doi.org/10.57760/sciencedb.07093>



**Figure 1.** Peak intensity distribution and peak intensity ratio pixel by pixel measured in the  $^{12}\text{CO}$ ,  $^{13}\text{CO}$ , and  $\text{C}^{18}\text{O}$  catalog. The color coding represents the distribution of the probability density functions of the pixels with  $^{13}\text{CO}$  emission (2D probability density functions), which are calculated by utilizing kernel density estimation through Gaussian kernels in the Python package `scipy.stats.Gaussian_kde` ([https://docs.scipy.org/doc/scipy/reference/generated/scipy.stats.Gaussian\\_kde.html](https://docs.scipy.org/doc/scipy/reference/generated/scipy.stats.Gaussian_kde.html)).

### 3.2. Optical Depth

On the other hand, the optical depth of the  $^{13}\text{CO}$  and  $\text{C}^{18}\text{O}$  emission can be derived as follows (Pineda et al. 2010):

$$\tau(^{13}\text{CO}) = -\ln \left[ 1 - \frac{T_{\text{mb}}(^{13}\text{CO})}{5.29} (e^{5.29/T_{\text{ex}}} - 1)^{-1} - 0.164 \right]^{-1} \quad (3)$$

$$\tau(\text{C}^{18}\text{O}) = -\ln \left[ 1 - \frac{T_{\text{mb}}(\text{C}^{18}\text{O})}{5.27} (e^{5.27/T_{\text{ex}}} - 1)^{-1} - 0.166 \right]^{-1}. \quad (4)$$

The variation of  $\tau(^{13}\text{CO})$  with the  $^{13}\text{CO}$  integrated intensity is shown in Figure 2. The dispersion of  $\tau(^{13}\text{CO})$  decreases rapidly with the  $^{13}\text{CO}$  integrated intensity. For about 70% of pixels,  $\tau(^{13}\text{CO})$  falls within the range of [0.1, 0.4].

Assuming typical relative abundances for the CO isotopologues in the local ISM ( $X_{^{12}\text{CO}}/X_{^{13}\text{CO}} = 89$ ; Lang 1980), the opacity  $\tau(^{12}\text{CO})$  can be easily obtained from  $\tau(^{13}\text{CO})$  by multiplying the ratio  $X_{^{12}\text{CO}}/X_{^{13}\text{CO}}$  (Figure 2). This shows that almost all the  $^{12}\text{CO}$  is optically thick ( $\tau(^{12}\text{CO}) > 1$ ), with 77% of pixels falling within the  $\tau(^{12}\text{CO})$  range of [10, 40]. This indicates that the approximate relation of Equation (2) is valid in most clouds. It is important to note that  $\tau(^{12}\text{CO})$  is derived from  $\tau(^{13}\text{CO})$ , so we cannot obtain  $\tau(^{12}\text{CO})$  values in some

diffuse regions where  $^{13}\text{CO}$  emission is not detected, and these  $\tau(^{12}\text{CO})$  results are not included in our diagram (Figure 2).

According to Equation (4), the  $\tau(\text{C}^{18}\text{O})$  results for the 32-cloud catalog with  $\text{C}^{18}\text{O}$  emission are shown in Figure 2. The dispersion of  $\tau(\text{C}^{18}\text{O})$  decreases with the  $\text{C}^{18}\text{O}$  emission and remains within the range of [0.05, 0.1]. The value of  $\tau(\text{C}^{18}\text{O})$  is concentrated between 0.04 and 0.2 for more than 90% of pixels, which is much smaller than the values of  $\tau(^{12}\text{CO})$  and  $\tau(^{13}\text{CO})$ . This suggests that in most clouds,  $\text{C}^{18}\text{O}$  is optically thin.

### 3.3. Integrated Intensity

Figure 3 shows the relationship between the integrated intensity of  $^{12}\text{CO}$  and  $^{13}\text{CO}$  in the 1197-cloud catalog. The  $^{12}\text{CO}$  intensity is in the range of [0.86, 206.25]  $\text{K km s}^{-1}$ , and the  $^{13}\text{CO}$  is in the range of [0.38, 57.93]  $\text{K km s}^{-1}$  (Table 1). 80.8% pixels have the intensity of  $^{12}\text{CO}$  and  $^{13}\text{CO}$  in the ranges of [1, 30]  $\text{K km s}^{-1}$  and [0.4, 5]  $\text{K km s}^{-1}$ , respectively. The  $^{13}\text{CO}$  intensity is increasing with the  $^{12}\text{CO}$  emission, while the slope ( $I^{13\text{CO}}/I^{12\text{CO}}$ ) slowly increases from 0.15 to 0.25 with the  $^{12}\text{CO}$  intensity. The change in the growth slope may be caused by two reasons: one is the increase in the optical depth of  $^{12}\text{CO}$  in the high-intensity region, which results in the decrease of the  $^{12}\text{CO}$  intensity, and the other is the increase in the  $^{13}\text{CO}$  intensity due to the self-shielding effect.

Figure 3 presents the ratio  $I^{13\text{CO}}/I^{12\text{CO}}$  in the 1197-cloud catalog. The scatter of the ratio is decreasing with  $I^{12\text{CO}}$  and is

**Table 1**  
A Catalog of Observational Properties

|      | $T_{\text{peak}}^{12}$<br>(K) | $T_{\text{peak}}^{13}$<br>(K) | $T_{\text{peak}}^{18}$<br>(K) | $T_{\text{ex}}$<br>(K) | $\tau_{12}$ | $\tau_{13}$ | $\tau_{18}$ | $I_{12}$<br>(K km s <sup>-1</sup> ) | $I_{13}$<br>(K km s <sup>-1</sup> ) | $I_{18}$<br>(K km s <sup>-1</sup> ) | $A_{12}$<br>(arcmin <sup>2</sup> ) | $A_{13}$<br>(arcmin <sup>2</sup> ) | $A_{18}$<br>(arcmin <sup>2</sup> ) |
|------|-------------------------------|-------------------------------|-------------------------------|------------------------|-------------|-------------|-------------|-------------------------------------|-------------------------------------|-------------------------------------|------------------------------------|------------------------------------|------------------------------------|
| Min  | 1.4759                        | 0.6658                        | 0.7759                        | 4.5090                 | 4.8559      | 0.0546      | 0.0279      | 0.8614                              | 0.3821                              | 0.5701                              | 1.0000                             | 0.5000                             | 0.5000                             |
| Max  | 37.5405                       | 15.1960                       | 3.5308                        | 41.0634                | 309.9523    | 3.4826      | 0.6116      | 206.2471                            | 57.9293                             | 11.6475                             | 35751.7500                         | 18171.0000                         | 1028.0000                          |
| Mean | 6.8713                        | 1.9809                        | 1.3343                        | 10.1883                | 32.0960     | 0.3606      | 0.1190      | 19.1297                             | 3.3174                              | 1.9735                              | 44.6266                            | 45.3179                            | 48.9141                            |

**Note.** The columns show the peak intensity, excitation temperature, optical depth, integrated intensity, and emission for <sup>12</sup>CO, <sup>13</sup>CO, and C<sup>18</sup>O, respectively. The rows are the minimum, maximum, and mean values of the corresponding parameters.



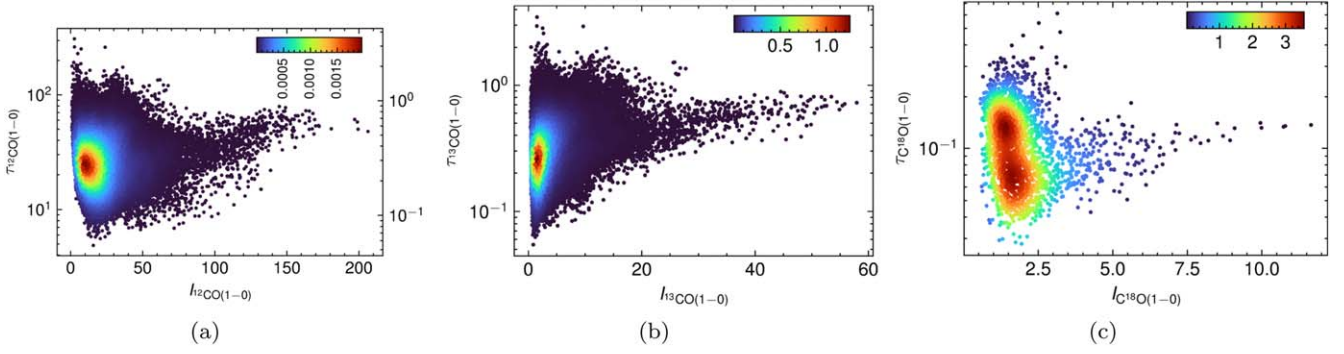


**Figure 2.** Optical depth  $\tau$  vs. velocity-integrated intensity  $I$ , pixel by pixel, measured in the  $^{12}\text{CO}$ ,  $^{13}\text{CO}$ , and  $\text{C}^{18}\text{O}$  catalog. The color coding is the same as in Figure 1.

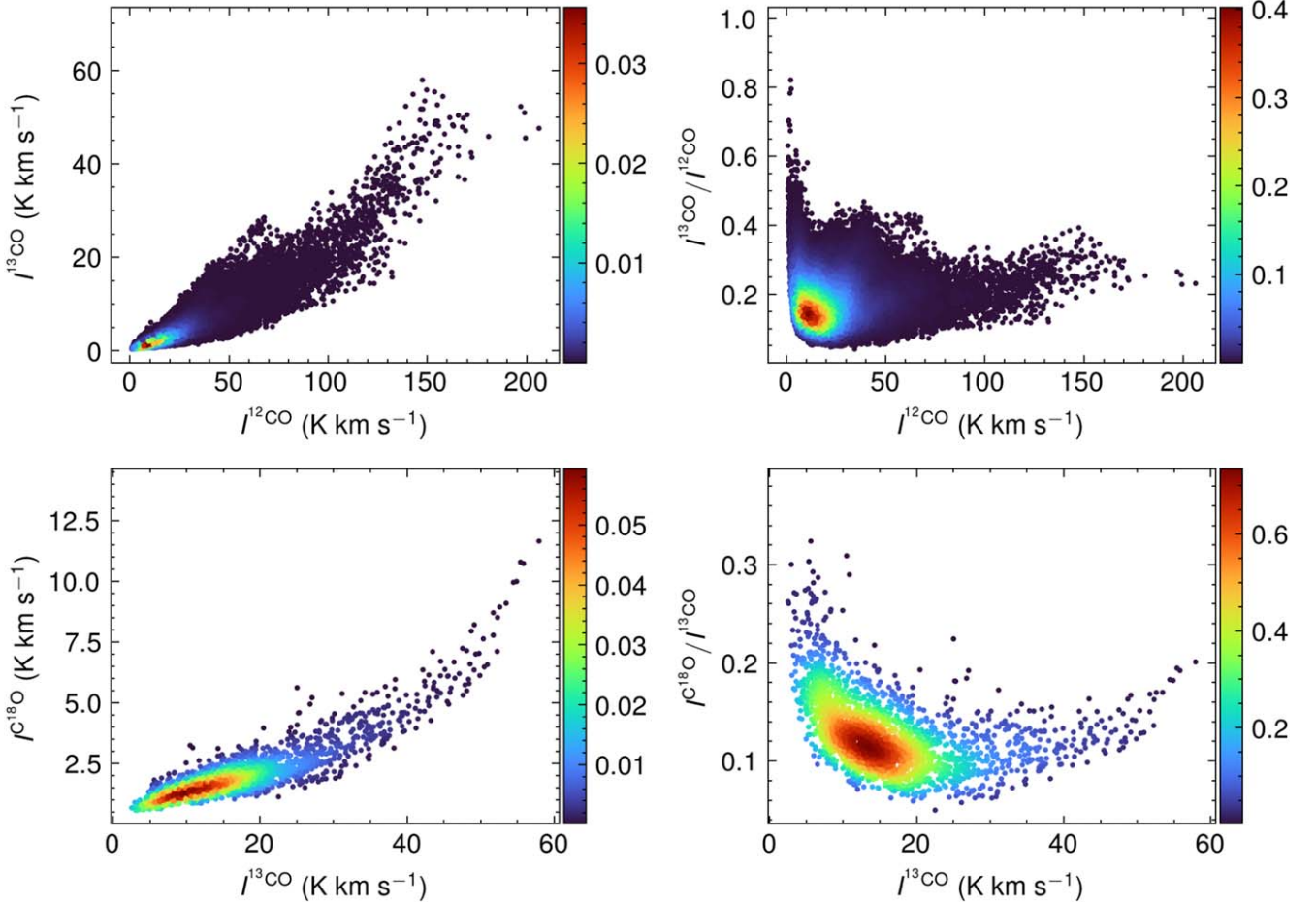


**Figure 3.** Intensity distribution between  $^{12}\text{CO}$ ,  $^{13}\text{CO}$ , and  $\text{C}^{18}\text{O}$ , pixel by pixel. The color coding is the same as in Figure 1.

concentrated on  $\sim 0.3$  in the high-intensity region. Different than the high-intensity region distribution, 73.38% of pixels have the ratio  $I^{13\text{CO}}/I^{12\text{CO}}$  in the range of  $[0, 0.2]$ .

The relationship between the integrated intensity of  $^{13}\text{CO}$  and  $\text{C}^{18}\text{O}$  in the 32-cloud catalog is presented in Figure 3. The  $\text{C}^{18}\text{O}$  intensity is in the range of  $[0.57, 11.65]$   $\text{K km s}^{-1}$ . Similar to  $^{12}\text{CO}$  against  $^{13}\text{CO}$ , the  $\text{C}^{18}\text{O}$  intensity is increasing with the  $^{13}\text{CO}$  emission, and the slope becomes steeper after the  $^{13}\text{CO}$  intensity is greater than  $40$   $\text{K km s}^{-1}$ . The ratio  $I^{\text{C}^{18}\text{O}}/I^{13\text{CO}}$  is decreasing with  $I^{13\text{CO}}$  in the low-intensity region, but increasing with  $I^{13\text{CO}}$  in the high-intensity region (Figure 3). The ratio  $I^{\text{C}^{18}\text{O}}/I^{13\text{CO}}$  is concentrated on  $[0.05, 0.15]$ . As

discussed in Section 4, the change in the slope may be related to selective FUV photodissociation (Hollenbach & Tielens 1997) and self-shielding effects (van Dishoeck & Black 1988; Warin et al. 1996; Liszt 2007; Visser et al. 2009; Shimajiri et al. 2014, 2015).

### 3.4. Angular Area

Figure 4 shows the relationship between the angular areas of  $^{12}\text{CO}$  and  $^{13}\text{CO}$  emission. The angular area of  $^{13}\text{CO}$  ( $A^{13\text{CO}}$ ) increases with  $A^{12\text{CO}}$  and its dispersion decreases. Interestingly, there appears to be an upper ratio of 0.7, with the area ratio of  $^{13}\text{CO}$  to  $^{12}\text{CO}$  approaching 0.7 as the cloud area increases.

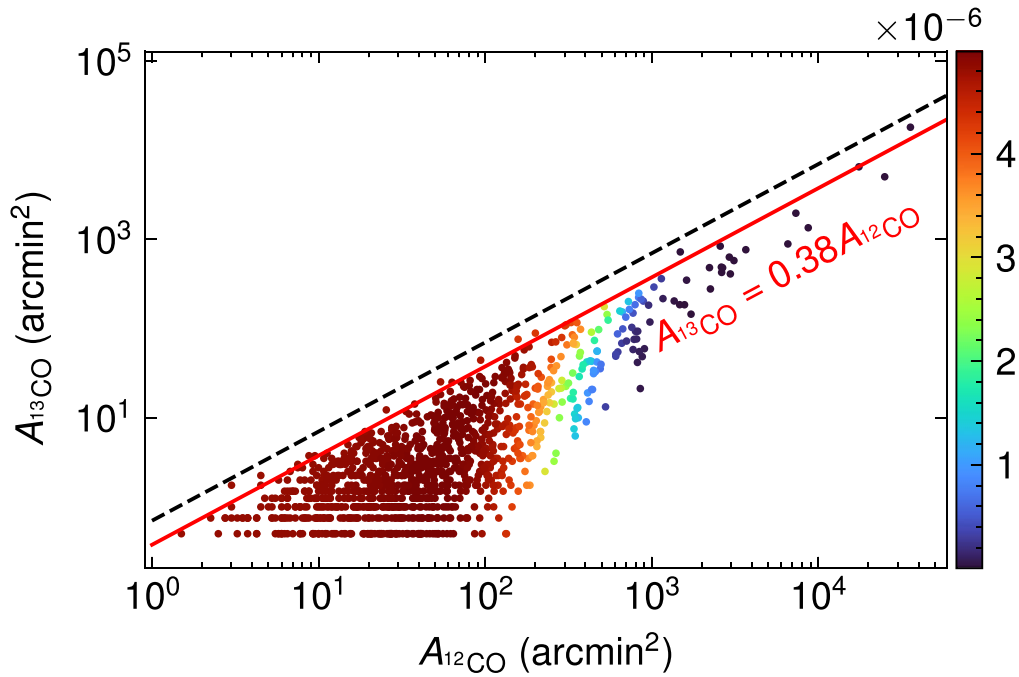


**Figure 4.**  $^{13}\text{CO}$  area vs.  $^{12}\text{CO}$  area cloud by cloud, measured in the 1197-cloud catalog. The color coding is the same as in Figure 1. The red line represents a linear fit with a ratio of 0.38. The fitting is calculated by utilizing the OLS function in the Python package Statsmodels ([https://www.statsmodels.org/dev/generated/statsmodels.regression.linear\\_model.OLS.html](https://www.statsmodels.org/dev/generated/statsmodels.regression.linear_model.OLS.html)), assuming a zero intercept and no weighting. The dashed black line is the limit with a ratio of 0.7 proposed by Yuan et al. (2022).

Yuan et al. (2022) also found that the area of  $^{13}\text{CO}$  emission in an MC generally does not exceed 70% of the  $^{12}\text{CO}$  emission area, based on the second Galactic quadrant from the same MWISP project. Figure 4 confirms that our sample is also within this limit of the 0.7 ratio. Through linear fitting of the data, the angular area ratio of  $^{12}\text{CO}$  and  $^{13}\text{CO}$  can be obtained as 0.38. The fitting calculated by utilizing the ordinary least squares (OLS) function in the Python package Statsmodels, assuming a zero intercept and no weighting. It should be noted that our fit is performed in a linear space, whereas Figure 4 shows a distribution in a logarithmic space. Therefore, in Figure 4, there are some MCs at the bottom left that deviate from the fitted line with a large difference, but in the actual linear space, they differ little from the fitted line. The value of the ratio of 0.38 may be related to the sensitivity of the data, which will be discussed in detail in our next work (C. Wang et al. 2023, in preparation). Sun et al. (2020) found that the ratios of  $A_{^{13}\text{CO}}$  to  $A_{^{12}\text{CO}}$  vary from 0.04 to 0.26 in different Galactic arms, based on the same data of MWISP over  $l = [129^\circ.75, 140^\circ.25]$ . This suggests that the distance factor has a significant effect on the ratio. It is noted that the areas of  $^{12}\text{CO}$  and  $^{13}\text{CO}$  emission have a large dispersion in the region where  $A_{^{13}\text{CO}}$  is less than  $10^3$  arcmin $^2$ . This could be caused by the filling factor or sensitivity, as discussed in Section 6.2. The beam filling factor is mainly correlated with the angular size, which makes the  $^{13}\text{CO}$  signal more difficult to detect in smaller MCs. Therefore, for small-angular-area MCs, the area detection of  $^{13}\text{CO}$  is seriously underestimated. This also explains why the  $A_{^{13}\text{CO}}$  of MCs with smaller angular areas is basically much smaller than the result from linear fitting.

### 3.5. Flux

In order to clarify the MC regions discussed, we divide the MC into three parts, based on the CO isotopologue emission

characteristics:  $^{12}\text{CO}$ -only,  $^{13}\text{CO}$ -bright, and  $\text{C}^{18}\text{O}$ -bright.  $^{12}\text{CO}$ -only represents a region with only  $^{12}\text{CO}$  emission and no  $^{13}\text{CO}$  and  $\text{C}^{18}\text{O}$  detected.  $^{13}\text{CO}$ -bright represents a region with  $^{12}\text{CO}$  and  $^{13}\text{CO}$  emission, but no  $\text{C}^{18}\text{O}$  detected. Finally,  $\text{C}^{18}\text{O}$ -bright is a region in which all of the CO isotopologues are detected.

A strong correlation between the flux of  $^{12}\text{CO}$  and  $^{13}\text{CO}$  in the  $^{13}\text{CO}$ -bright region can be found in Figure 5, spanning six orders of magnitude. It should be noted that the  $^{12}\text{CO}$  flux in Figure 5 only includes the  $^{13}\text{CO}$ -bright region, but does not include the diffuse region with only  $^{12}\text{CO}$  emission. Despite the large optical depth ratios of  $^{12}\text{CO}$  to  $^{13}\text{CO}$ , it is interesting that the observed flux ratios are tightly correlated over such a wide range. We divide the MCs into hot and cold clouds, based on a maximum excitation temperature of 14 K. Figure 5 shows that hot clouds have higher flux values of  $^{12}\text{CO}$  and  $^{13}\text{CO}$  compared to cold clouds, but the flux ratio remains the same.

In general, for an optically thin molecular line, the flux of the molecular line is proportional to the mass of the molecule, and the flux of  $^{12}\text{CO}$  is proportional to the total mass of the cloud, thanks to the X-factor (Dame et al. 2001; Bolatto et al. 2013). The strong correlation in Figure 5 indicates that the MC in the section of the third Galactic quadrant has a stable and uniform  $^{13}\text{CO}$  abundance value (Section 4), and it also suggests that the value of the X-factor is statistically stable at the overall scale of the MC (Section 6.1). Through linear fitting of the data, we find that the data perfectly fit the relation  $F_{^{13}\text{CO}} = 0.17 F_{^{12}\text{CO}}$ . Since the majority of pixels have a ratio  $I_{^{13}\text{CO}}/I_{^{12}\text{CO}}$  in the range of [0, 0.2] and a  $^{12}\text{CO}$  intensity in the range of [0, 30] K km s $^{-1}$  (Figure 3), the relation  $F_{^{13}\text{CO}} = 0.17 F_{^{12}\text{CO}}$  indicates that the abundance  $X_{^{13}\text{CO}}$  is a constant for the entire sample (Section 4).

Another similarly strong correlation between the flux of  $^{13}\text{CO}$  and  $\text{C}^{18}\text{O}$  is also found in Figure 5. It should be noted that the  $^{13}\text{CO}$  flux here only includes the region in the MC with  $\text{C}^{18}\text{O}$  emission. Similar to Figure 5, hot clouds have higher flux

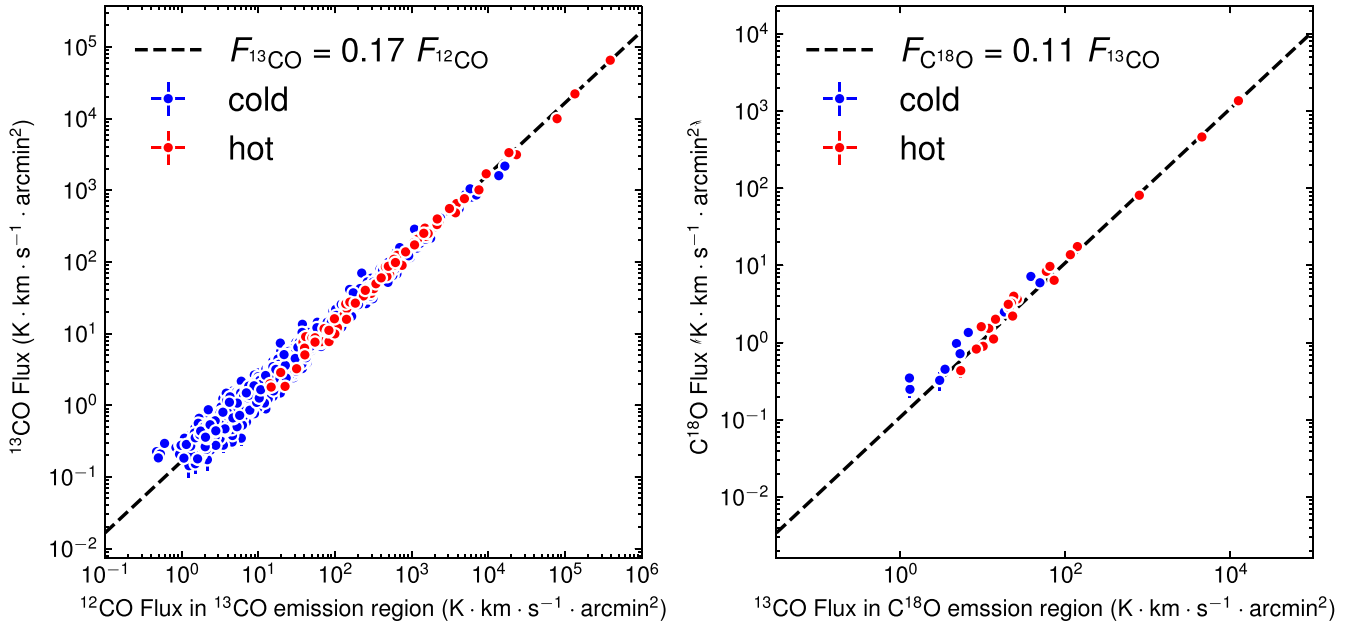


**Figure 5.** Left: flux ( $^{12}\text{CO}$ ) vs. flux ( $^{13}\text{CO}$ ) measured cloud by cloud in the 1197-cloud catalog. The flux ( $^{12}\text{CO}$ ) and flux ( $^{13}\text{CO}$ ) are calculated toward the same areas, where both  $^{12}\text{CO}$  and  $^{13}\text{CO}$  emissions are detected. Right: flux ( $^{13}\text{CO}$ ) vs. flux ( $\text{C}^{18}\text{O}$ ) measured in the 32-cloud catalog. The flux ( $^{13}\text{CO}$ ) and flux ( $\text{C}^{18}\text{O}$ ) are calculated toward the same areas, where both  $^{13}\text{CO}$  and  $\text{C}^{18}\text{O}$  emissions are detected. The colors indicate different types of MCs, based on excitation temperature.

values than cold clouds, but the flux ratio remains the same. Through linear fitting of the data, we find that the data perfectly fit the relation  $F_{\text{C}^{18}\text{O}} = 0.11 F_{^{13}\text{CO}}$ . This is consistent with Figure 3, which shows that the ratio  $I^{\text{C}^{18}\text{O}}/I^{^{13}\text{CO}}$  is concentrated in the range of [0.05, 0.15]. Such consistent flux ratios suggest that the abundance ratio  $X_{^{13}\text{CO}}/X_{\text{C}^{18}\text{O}}$  is a constant at the MC scale.

In general, the column density of  $^{13}\text{CO}$  and  $\text{C}^{18}\text{O}$  in an MC can be calculated from the integral intensity of an optically thin MC line, if the excitation temperature of the cloud is known (Garden et al. 1991; Bourke et al. 1997). The column density equations for  $^{13}\text{CO}$  and  $\text{C}^{18}\text{O}$  are given by:

$$N(^{13}\text{CO}) = 2.42 \times 10^{14} \frac{\tau(^{13}\text{CO})}{1 - e^{-\tau(^{13}\text{CO})}} \frac{1 + 0.88/T_{\text{ex}}}{1 - e^{-5.29/T_{\text{ex}}}} \times \int T_{\text{mb}}(^{13}\text{CO}) dv, \quad (5)$$

$$N(\text{C}^{18}\text{O}) = 2.54 \times 10^{14} \frac{\tau(\text{C}^{18}\text{O})}{1 - e^{-\tau(\text{C}^{18}\text{O})}} \frac{1 + 0.88/T_{\text{ex}}}{1 - e^{-5.27/T_{\text{ex}}}} \times \int T_{\text{mb}}(\text{C}^{18}\text{O}) dv. \quad (6)$$

So the flux ratio  $F_{\text{C}^{18}\text{O}}/F_{^{13}\text{CO}}$  can be derived as:

$$\frac{F_{\text{C}^{18}\text{O}}}{F_{^{13}\text{CO}}} = \frac{2.42 \times 10^{14}}{2.54 \times 10^{14}} \times \frac{M(\text{C}^{18}\text{O})}{M(^{13}\text{CO})} \times \frac{\tau(^{13}\text{CO})}{1 - e^{-\tau(^{13}\text{CO})}} \frac{1 - e^{-\tau(\text{C}^{18}\text{O})}}{\tau(\text{C}^{18}\text{O})}. \quad (7)$$

Here,  $M(^{13}\text{CO})$  and  $M(\text{C}^{18}\text{O})$  represent the masses of  $^{13}\text{CO}$  and  $\text{C}^{18}\text{O}$  in the cloud, respectively. It is observed that in the third Galactic quadrant, the abundance ratio of  $X_{^{13}\text{CO}}/X_{\text{C}^{18}\text{O}}$  ( $= M(^{13}\text{CO})/M(\text{C}^{18}\text{O})$ ) is a constant of  $9.7_{-0.8}^{+0.6}$  (the error is derived from the change in optical depth) on the MC scale, calculated from Equation (7), and the values of the relation  $F_{\text{C}^{18}\text{O}} = 0.11 F_{^{13}\text{CO}}$  based on the mean optical thicknesses of  $^{13}\text{CO}$  and  $\text{C}^{18}\text{O}$  (Table 1) are 0.36 and 0.12, respectively. This former value is nearly twice as high as the terrestrial ratio of 5.5

(Wilson & Matteucci 1992). This result is consistent with the findings shown in Figure 7, which indicates that  $X_{^{13}\text{CO}}/X_{\text{C}^{18}\text{O}}$  inside the cloud is concentrated (90.6%) in the interval [5, 18]. The value of  $X_{^{13}\text{CO}}/X_{\text{C}^{18}\text{O}}$  as  $9.7_{-0.8}^{+0.6}$  falls between the Planck cold clumps of the ECC catalog with a value of 7 (Wu et al. 2012) and the Orion A giant MC (except for photon-dominated regions) with a value of 12.29 (Shimajiri et al. 2014). Since our sample contains MCs that may be in different evolutionary stages, such as cold clouds and hot clouds, this stable abundance ratio indicates that the isotope abundance ratio remains constant at the overall scale of MCs during the evolution of MCs. It is not unique; Romano et al. (2017) and Sliwa et al. (2017) have shown that known photochemical effects (selective photodissociation and fractionation) cannot induce global isotopologue abundances to differ from the intrinsic, initial-mass-function-determined, isotopic abundances in star-forming galaxies.

#### 4. Abundance $X_{^{13}\text{CO}}$

As shown in Section 3.5, the  $^{13}\text{CO}$  column density of the cloud can be obtained with Equation (5). On the other hand, the column density of  $\text{H}_2$  in each pixel can be obtained from  $^{12}\text{CO}$  emission, thanks to the X-factor (Dame et al. 2001; Bolatto et al. 2013):

$$N(\text{H}_2) = X \times I_{^{12}\text{CO}}. \quad (8)$$

So, the flux ratio  $F_{^{13}\text{CO}}/F_{^{12}\text{CO}}$  can be derived:

$$\frac{F_{^{13}\text{CO}}}{F_{^{12}\text{CO}}} = \frac{M(^{13}\text{CO})}{M(\text{H}_2)} \frac{X}{2.42 \times 10^{14}} \frac{1 - e^{-\tau(^{13}\text{CO})}}{\tau(^{13}\text{CO})} \frac{1 - e^{-5.29/T_{\text{ex}}}}{1 + 0.88/T_{\text{ex}}}. \quad (9)$$

Here,  $M(^{13}\text{CO})$  is the mass of  $^{13}\text{CO}$  in the cloud and  $M(\text{H}_2)$  is the mass of  $\text{H}_2$  in the cloud. The ratio between  $M(^{13}\text{CO})$  and  $M(\text{H}_2)$  represents the abundance of  $^{13}\text{CO}$ , denoted as  $X_{^{13}\text{CO}}$ , in the cloud. As shown in Section 3.1, the optical depth  $\tau(^{13}\text{CO})$  of most molecular gases is concentrated around 0.1, and the

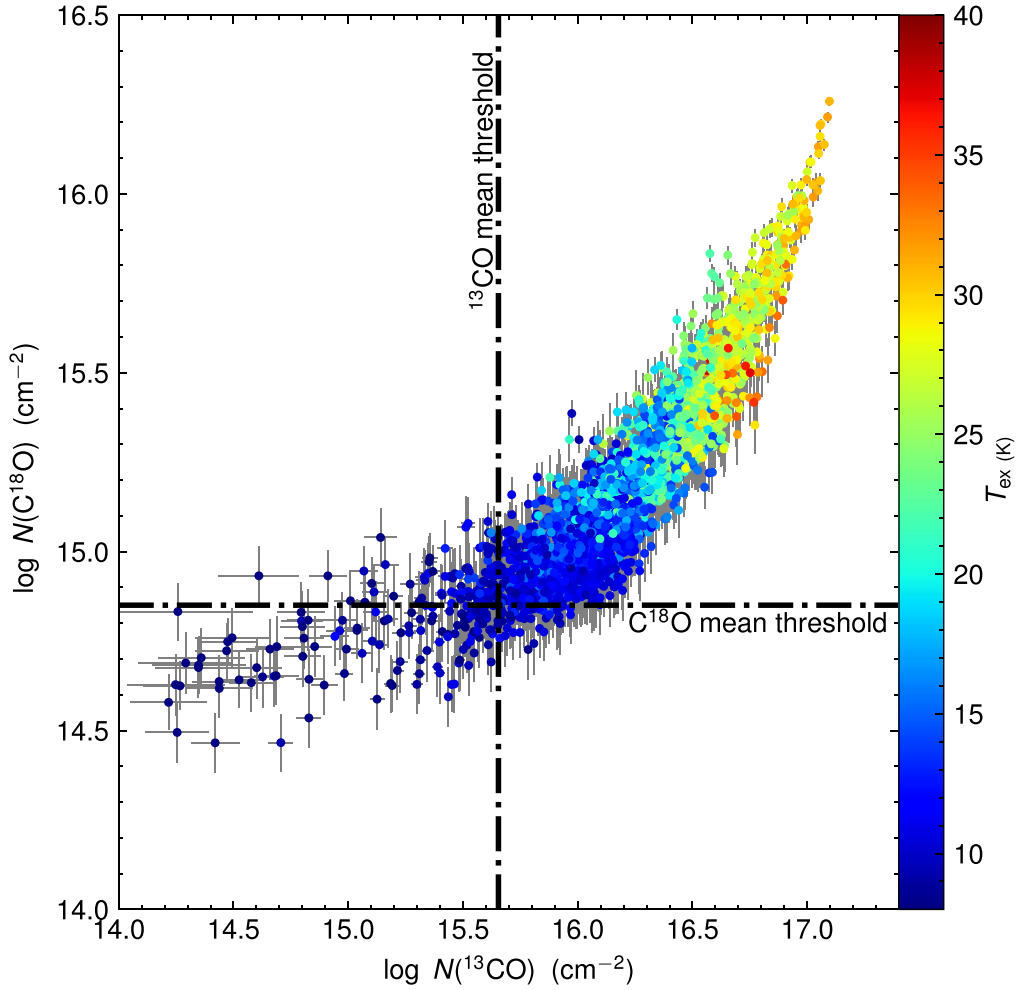


**Figure 6.**  $N_{^{13}\text{CO}}$  vs.  $N_{\text{C}^{18}\text{O}}$  pixel by pixel measured in 32 clouds. The color coding shows the excitation temperature derived from the  $^{12}\text{CO}$  peak intensity. The two dashed lines show the mean threshold of the integrated intensity noise, which corresponds to  $N_{^{13}\text{CO}}$  and  $N_{\text{C}^{18}\text{O}}$  of  $4.5 \times 10^{15} \text{ cm}^{-2}$  and  $7.0 \times 10^{14} \text{ cm}^{-2}$ , respectively. The gray lines show the error bar for each pixel.

peak temperature  $T_{\text{peak}}^{^{12}\text{CO}}$  is around 10 K, corresponding to an excitation temperature of 13.4 K. Therefore, the value of  $X_{^{13}\text{CO}}$  is estimated to be  $6.5_{-0.5}^{+0.1} \times 10^{-7}$  (the error is derived from the change in optical depth) based on the  $F_{^{13}\text{CO}}/F_{^{12}\text{CO}}$  value of 0.17 and the X-factor ( $2 \times 10^{20} \text{ cm}^{-2} (\text{K km s}^{-1})^{-1}$ ; Bolatto et al. 2013).

The findings from Milam et al. (2005) and Wang et al. (2019) suggest that there may be variations in the  $^{12}\text{C}/^{13}\text{C}$  ratio and  $X_{^{13}\text{CO}}$  value in different regions of MCs and with Galactic distance. However, our results show that, overall, the  $X_{^{13}\text{CO}}$  value remains stable at a fixed value without significant distance variation, and there is no obvious relationship with the local environment and evolution. This implies that although there may be local changes in MC properties due to star-forming activities and other factors, the overall properties of MCs remain relatively stable. This is consistent with the discussion of  $X_{^{13}\text{CO}}/X_{\text{C}^{18}\text{O}}$  in the next section, suggesting that MCs hold a constant  $X_{^{13}\text{CO}}/X_{\text{C}^{18}\text{O}}$  ratio, despite local variations inside. It should be noted that this conclusion is based on the premise of the LTE assumption and the assumption that the X-factor is generally true and maintains a fixed value. Meanwhile, we assume that the MC has a relatively consistent  $\tau(^{13}\text{CO})$  and excitation temperature. However, as the correlated axes will induce a potentially strong bias, we remain cautious

about the result of a constant abundance  $X_{^{13}\text{CO}}$  over the sample. Interestingly, the linear relationship between the  $^{12}\text{CO}$  and  $^{13}\text{CO}$  flux holds not only for the  $^{13}\text{CO}$ -bright region, but also for the entire MC scale (Section 6.4). This will also be further studied in detail in our next work (Wang et al. 2023, in preparation).

## 5. Abundance Ratio $X_{^{13}\text{CO}}/X_{\text{C}^{18}\text{O}}$

Figure 6 shows the pixel-by-pixel plot of  $N_{^{13}\text{CO}}$  versus  $N_{\text{C}^{18}\text{O}}$  for the 32-cloud sample. The pixel selection is the same as the results presented in Section 3.1. It can be observed from Figure 6 that the distributions of  $N(^{13}\text{CO})$ ,  $N(\text{C}^{18}\text{O})$ , and  $T_{\text{ex}}$  are closely related.  $N(\text{C}^{18}\text{O})$  and  $T_{\text{ex}}$  increase with increasing  $N(^{13}\text{CO})$ , and all three show a simple, monotonically increasing correlation. Since the intensity noise  $\sigma_i$  is related to the velocity range of integration, and the velocity range of each MC is quite different, the noise  $\sigma_i$  of each pixel is also different. We calculate the mean threshold of the integrated intensity noise, which corresponds to  $N_{^{13}\text{CO}}$  and  $N_{\text{C}^{18}\text{O}}$  of  $4.5 \times 10^{15} \text{ cm}^{-2}$  and  $7.0 \times 10^{14} \text{ cm}^{-2}$ , respectively. Data points below the mean threshold need to be treated with care, as they may have large error and selection effects. It should be noted that the threshold describes where the distribution seen in Figure 6 will not be properly sampled anymore. This could be why the curve seems



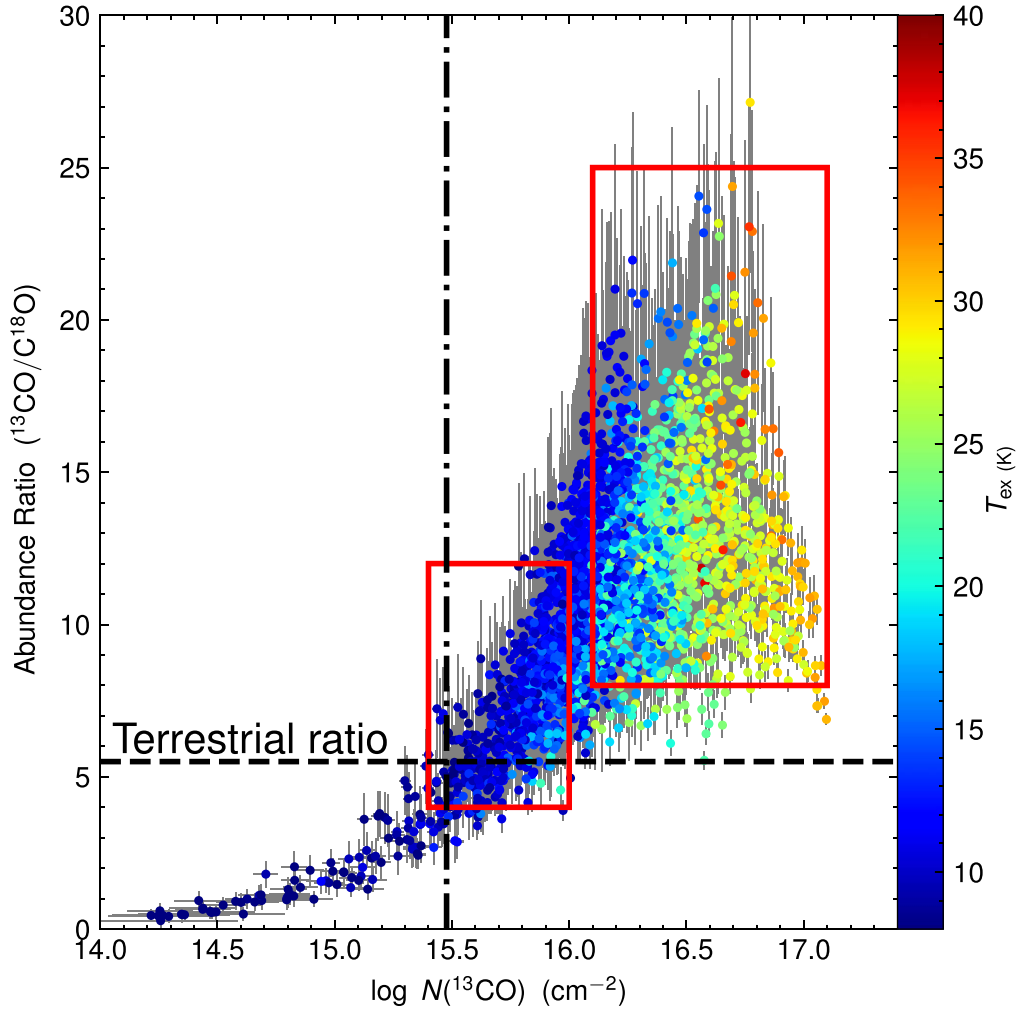
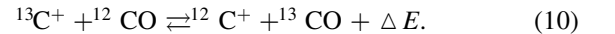


**Figure 7.**  $N_{13\text{CO}}$  vs.  $X_{13\text{CO}}/X_{\text{C}^{18}\text{O}}$  pixel by pixel measured in 32 clouds. The color coding shows the excitation temperature derived from the  $^{12}\text{CO}$  peak intensity. The two dashed lines show the mean threshold of  $\text{C}^{18}\text{O}$   $7.0 \times 10^{14} \text{ cm}^{-2}$  and the terrestrial ratio  $X_{13\text{CO}}/X_{\text{C}^{18}\text{O}}$  5.5 (Wilson & Matteucci 1992), respectively. The two red rectangles present two typical distribution regions of the Type I and Type II clouds classified in Wang et al. (2019). The gray lines show the error bar for each pixel.

to flatten off, since  $N(\text{C}^{18}\text{O})$  below  $10^{15} \text{ cm}^{-2}$  is hard to detect, due to the lower line intensity. We will verify this information by increasing the sensitivity in the future.

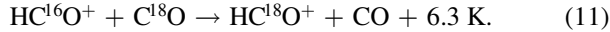
Figure 7 illustrates the correlation between  $N_{13\text{CO}}$  and the abundance ratio  $X_{13\text{CO}}/X_{\text{C}^{18}\text{O}}$  in clouds. The ratio displays a strong correlation with column density and temperature. Based on the temperature difference, there are obviously three distinct regions in the figure, corresponding to temperature intervals of [0, 14] K (cold), [14, 20] K (warm), and [20, 40] K (hot), respectively. The cold gas displays a wide range of  $N_{13\text{CO}}$  distribution, from  $1 \times 10^{14} \text{ cm}^{-2}$  to  $3.2 \times 10^{16} \text{ cm}^{-2}$  (minimum and maximum), while the warm and hot gases have narrower  $N_{13\text{CO}}$  ranges of  $[0.6, 3.2] \times 10^{16} \text{ cm}^{-2}$  and  $[1.6, 10] \times 10^{16} \text{ cm}^{-2}$ , respectively. Similarly, the  $X_{13\text{CO}}/X_{\text{C}^{18}\text{O}}$  distribution in the cold gas also has a wider range [0, 22], but with smaller dispersion, while the warm and hot gases concentrate in the range of 5–20, but with larger dispersion. Interestingly, the distribution of hot and cold gases is almost perfectly staggered in Figure 7, while the distribution of warm gas appears as a transition zone. In addition, as Figure 6 shows, the threshold describes where the distribution seen in the figure will not be properly sampled anymore. This could be why the data points below the threshold have very low abundance ratios.

If we focus on the cold gas distribution in Figure 7, the distribution follows the quadratic relation with respect to the  $^{13}\text{CO}$  column density. This is probably due to isotope fractionation reactions. As demonstrated by Szűcs et al. (2014), both isotopic species are effectively shielded from interstellar FUV photons in the dense region ( $2 \text{ mag} < A_V < 5 \text{ mag}$ ), due to the shielding effect of dust absorption and the increasing CO column density. This means that in the absence of additional heating sources, the  $N_{13\text{CO}}$  will increase in this region, due to self-shielding against the interstellar radiation field. On the other hand, ionized carbon remains abundant in this region, making the chemical fractionation reaction (Watson et al. 1976) important:



The rate coefficient for the left-to-right direction is  $R_{\text{frac,CO,lr}} = 2 \times 10^{-10} \text{ cm}^3 \text{ s}^{-1}$ , and for the other direction, it is  $R_{\text{frac,CO,rl}} = 2 \times 10^{-10} \exp(-35 \text{ K}/T_{\text{gas}}) \text{ cm}^3 \text{ s}^{-1}$ . This suggests that the effect of chemical fractionation depends only on temperature and not on density. The gas in this region typically has a temperature of  $\sim 10$  K. The exothermic reaction (to the right, leading to energy release) is preferred, resulting in more production of  $^{13}\text{CO}$ . Under the dual influence of  $^{13}\text{CO}$  self-shielding and chemical fractionation, the column density of

$^{13}\text{CO}$  significantly increases in this region. However, in denser regions ( $A_V > 5$  mag), the CO chemistry is governed by non-isotope-selective reactions, and hence the column density of  $^{13}\text{CO}$  is expected to decline. Meanwhile, photons play a relatively small role and induce very few  $^{18}\text{O}$  fractionation effects as a result of CO self-shielding in the dense regions (Lyons & Young 2005; Smith et al. 2009; Loison et al. 2019). Langer et al. (1984) developed the only  $^{18}\text{O}$  fractionation model that considers only a few isotopologues and only one fractionation reaction, namely



This means that the column density of  $\text{C}^{18}\text{O}$  may be reduced due to chemical fractionation at low temperatures. In fact, we observe that the  $X_{^{13}\text{CO}}/X_{\text{C}^{18}\text{O}}$  ratio of cold gas increases monotonically until the extinction value is 7. This clearly shows that the effect of chemical fractionation depends only on temperature, and the effect of chemical fractionation on the MC may be larger than expected.

In contrast, the distribution of hot and warm gas points in Figure 7 differs from that of the cold gas. These hot and warm points exhibit relatively higher mean  $X_{^{13}\text{CO}}/X_{\text{C}^{18}\text{O}}$  ratios (12.5 and 11.0, respectively) than the cold gas (9.36), but as the  $^{13}\text{CO}$  column density increases, so does the temperature. Previous studies of Orion A (Shimajiri et al. 2014) and the Gemini OB1 MC Complex (Wang et al. 2019) have shown that CO rare isotopologues associated with OB stars or H II regions are more effectively dissociated by FUV emission compared to CO. Based on the data presented in this paper, it is difficult to distinguish whether the observed deviation from chemical fractionation is due to increasing temperature or the effect of selective photodissociation. In future studies, we can investigate their effects on the model from different perspectives, such as changes in temperature and radiation, to better match the observed distribution of results presented in this paper.

Selective photodissociation and chemical fractionation are currently considered to be the main factors driving CO isotopologue abundance variations. Stellar nucleosynthesis also affects the CO isotopologue abundance variations, but on larger scales, such as Galactic chemical evolution. For example, in massive stars, extremely high temperatures due to gravitational collapse initiate the formation of  $^{12}\text{C}$  through the fusion of three alpha particles (Timmer et al. 1995). On the other hand, in asymptotic giant branch stars,  $^{13}\text{C}$  is a reaction intermediate in the carbon–nitrogen–oxygen cycle (Pagel 1997). The intermediate product,  $^{13}\text{C}$ , is mixed into the expanding atmosphere of the star and finally ejected into the ISM after convective mixing (known as “third dredge-up”; Herwig & Austin 2004). Milam et al. (2005) measure the  $^{12}\text{C}/^{13}\text{C}$  ratios in Galactic MCs by using the  $N=1-0$  transition of the CN radical. They found  $^{12}\text{C}/^{13}\text{C}$  has a gradient with Galactic distance that is a true indicator of Galactic chemical evolution. Due to the optical thickness of  $^{12}\text{CO}$ , we cannot directly determine its column density. It is difficult to obtain the  $^{12}\text{C}/^{13}\text{C}$  from the CO isotopologues alone. In this paper, we cannot exclude selective nucleosynthesis, which usually acts on larger scales, as a potential driver for changes in the abundance of the CO isotopologues. The selective photodissociation and chemical fractionation are typically the most important to consider on the cloud scale (Szűcs et al. 2014).

Wang et al. (2019) found that clouds can be classified into two types, based on their  $X_{^{13}\text{CO}}/X_{\text{C}^{18}\text{O}}$  ratios, and pointed out

that Type I clouds are likely at an earlier evolutionary stage compared to Type II clouds. Figure 7 presents the typical distribution regions of these two types of clouds. The figure confirms that gases in the Type I distribution region have lower temperatures, column densities, and abundance ratios. Furthermore, the gas temperature, column density, and abundance ratio gradually increase during the transition from the Type I to the Type II distribution region, suggesting a possible evolutionary sequence between the two types of gases.

As shown in Figure 7,  $X_{^{13}\text{CO}}/X_{\text{C}^{18}\text{O}}$  varies from 0 to 25 and is concentrated in the interval [5, 18]. Although the abundance ratio  $X_{^{13}\text{CO}}/X_{\text{C}^{18}\text{O}}$  may locally vary by several times within the MC due to local environmental factors, the results in Figure 5 indicate that the overall abundance ratio of the MC remains relatively constant at 9.7 and is not significantly affected by local changes in the physical environment.

## 6. Discussion

### 6.1. X-factor

Astronomers frequently use  $^{12}\text{CO}$  emission to estimate the mass of molecular gas through the X-factor (Dame et al. 2001; Bolatto et al. 2013). The standard methodology assumes a simple relationship between the observed  $^{12}\text{CO}$  intensity  $I^{12\text{CO}}$  and the column density of the molecular gas  $N(\text{H}_2)$ , as given by Equation (8).

A corollary of this relation arises from integrating over the emitting area:

$$M_{\text{mol}} = \alpha_{\text{CO}} L_{\text{CO}}. \quad (12)$$

Here,  $M_{\text{mol}}$  is in units of solar mass and  $L_{\text{CO}}$  is usually expressed in  $\text{K km s}^{-1} \text{pc}^2$  if the distance is known.  $\alpha_{\text{CO}}$  is simply a mass-to-light ratio and is also referred to as the CO-to- $\text{H}_2$  conversion factor (e.g., for  $X = 2 \times 10^{20} \text{ cm}^{-2} (\text{K km s}^{-1})^{-1}$ , the corresponding  $\alpha_{\text{CO}}$  is  $4.3 M_{\odot} (\text{K km s}^{-1} \text{pc}^2)^{-1}$ ; Bolatto et al. 2013).

On the other hand, for optically thin tracers like  $^{13}\text{CO}$ , there is also a relationship between the observed intensity  $I^{13\text{CO}}$  and the column density of the molecular gas  $N(\text{H}_2)$  based on the LTE assumption and a certain abundance (Garden et al. 1991; Bourke et al. 1997). Therefore, Figure 5 suggests that the abundance  $X(^{13}\text{CO})$  may be a constant value on the scale of the MC as a whole, spanning six orders of magnitude. Additionally, Figure 5 provides direct evidence for the existence of the CO-to- $\text{H}_2$  conversion factor  $\alpha_{\text{CO}}$  and offers a way to calculate it. However, due to the lack of distance information, we are unable to provide this value at present, and it will be investigated in our future work.

### 6.2. Observational Uncertainty

Sensitivity is an important parameter in observational uncertainty, which is generally determined by the rms value of the spectrum. As we mentioned in the statistical study of observations in Section 3, selection effects may occur due to sensitivity thresholds, which can lead to bias in our understanding of the results. In fact, in addition to sensitivity, the beam filling factor is also an important and often overlooked factor that affects the observation uncertainty. For example, beam filling factors are usually assumed to be unity (i.e., 1 in this paper) in the calculation of physical properties such as the excitation temperature, optical depth, and column density, but this is inaccurate and may introduce systematic errors.

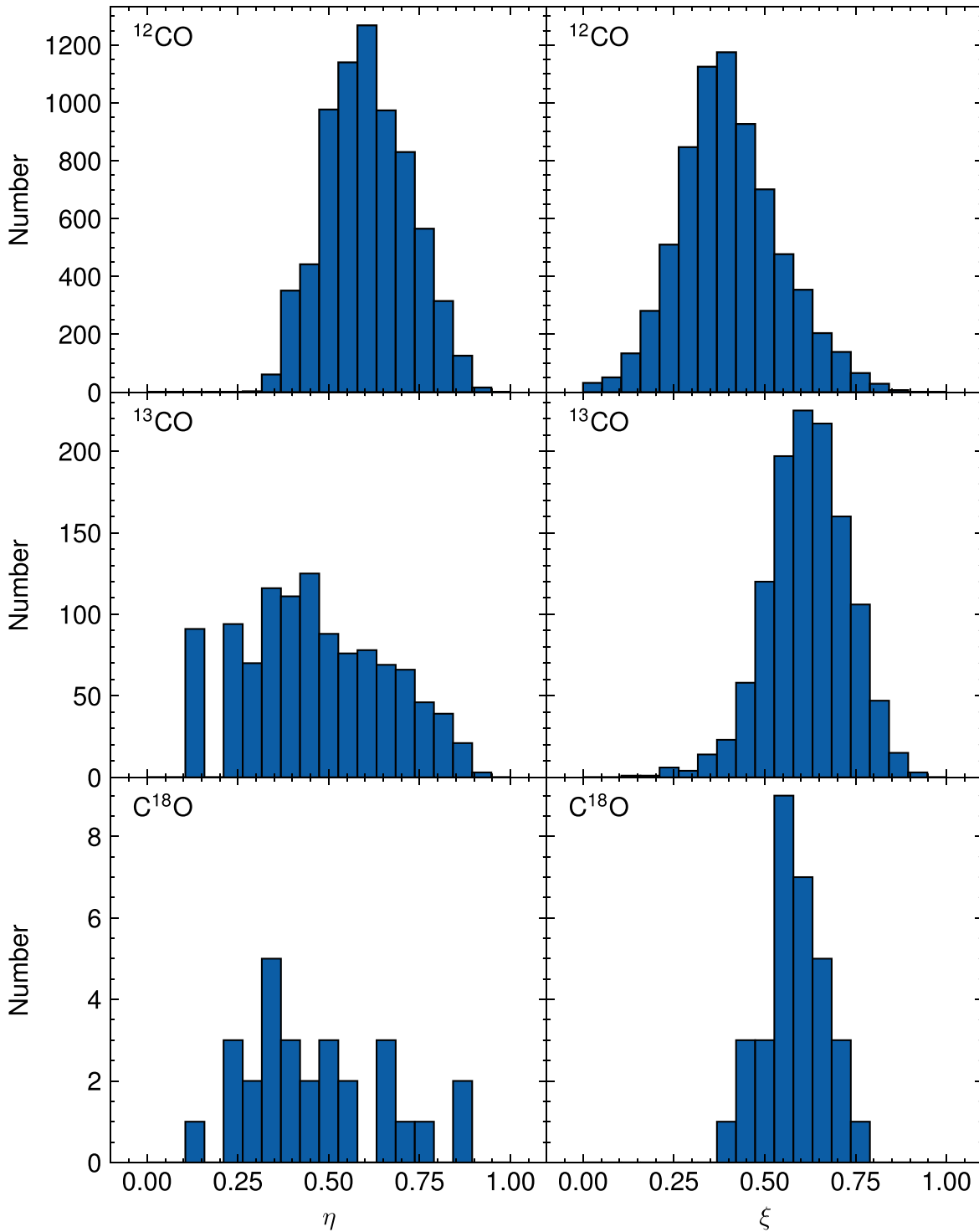


**Figure 8.** Histogram distribution of the filling factors  $\eta$  and sensitivity clip factors  $\xi$  for  $^{12}\text{CO}$ ,  $^{13}\text{CO}$ , and  $\text{C}^{18}\text{O}$  in the cloud catalog.

The beam filling factor  $\eta$  appears as a correction factor for the brightness temperature according to Equation (1). Yan et al. (2021) investigated the dependence of the beam filling factor on angular resolution, sensitivity (noise levels), distances, and molecular tracers using CO images of a large-scale region ( $25^\circ 8' < l < 49^\circ 7'$ ,  $|b| < 5^\circ$ ) mapped by the MWISP data. They found that the beam filling factors of  $^{12}\text{CO}$  and  $^{13}\text{CO}$  are approximately unity in the Local arm ( $\sim 1$  kpc), the Sagittarius arm ( $\sim 3$  kpc), and the Scutum arm ( $\sim 6$  kpc) for giant MCs, but drop to  $\sim 0.7$  and  $\sim 0.6$  in the Outer arm ( $\sim 15$  kpc),

respectively. However,  $\text{C}^{18}\text{O}$  decreases significantly with distance and becomes approximately zero in the Outer arm.

In addition to the distance factor, they found that the beam filling factor  $\eta$  is mainly correlated with the angular size  $\ell$  in beam size units and can be approximated by  $0.922\ell^2/(\ell + 0.762)^2$  (Yan et al. 2021). It should be noted that the sample of MCs with  $^{13}\text{CO}$  and  $\text{C}^{18}\text{O}$  emission was relatively small when they established this relationship, which makes it likely that the error will be large for  $^{13}\text{CO}$  and  $\text{C}^{18}\text{O}$  flux and  $\eta$ . We need to be careful with the corrected flux of

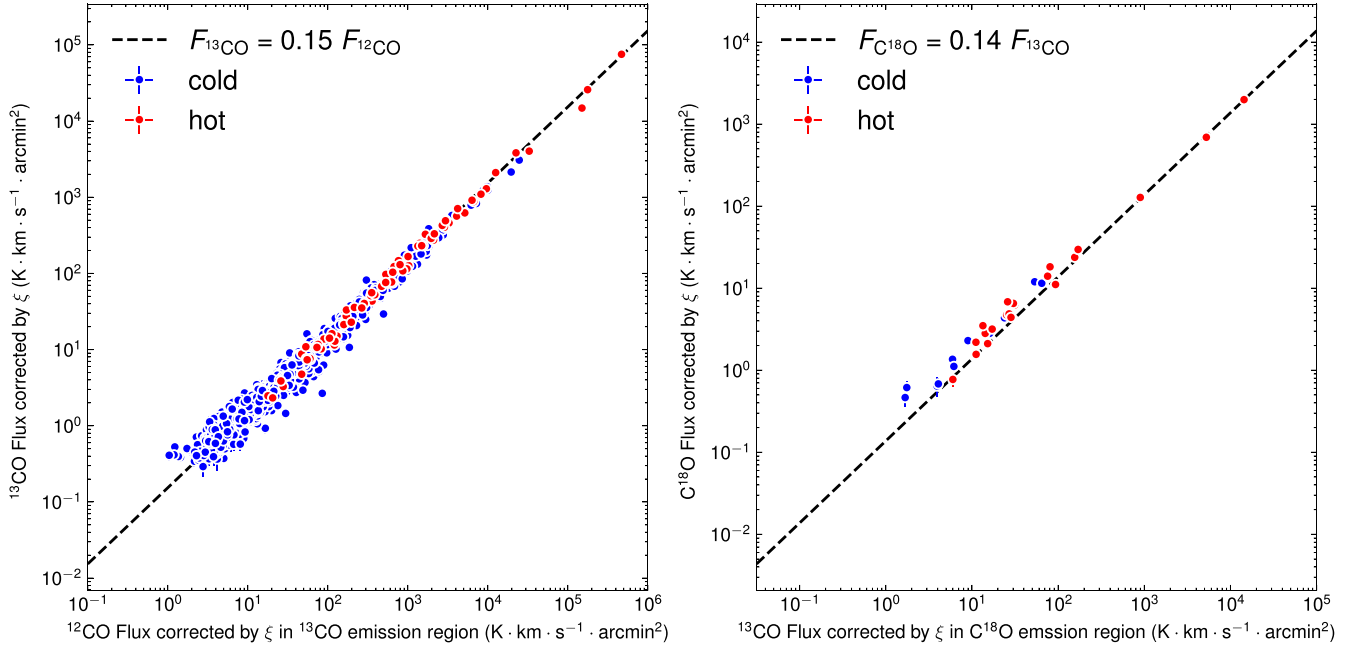


**Figure 9.** Left: corrected flux ( $^{12}\text{CO}$ ) vs. flux ( $^{13}\text{CO}$ ) cloud by cloud. Right: corrected flux ( $^{13}\text{CO}$ ) vs. flux ( $\text{C}^{18}\text{O}$ ) cloud by cloud. Different than Figure 5, the flux here is corrected based on the sensitivity clip factor  $\xi$ . The colors indicate different types of MCs, based on excitation temperature.

$^{13}\text{CO}$  and  $\text{C}^{18}\text{O}$ . The angular size is defined as the equivalent diameter derived from Equation (1):

$$\ell = \sqrt{\frac{4A}{\pi}} - \Theta, \quad (13)$$

where  $A$  is the angular area (presented in Section 3.4) and  $\Theta$  is the beam size of the MWISP survey. Figure 8 shows the histogram distribution of the beam filling factors for  $^{12}\text{CO}$ ,  $^{13}\text{CO}$ , and  $\text{C}^{18}\text{O}$  in the cloud catalog. It indicates that the  $\eta$  for  $^{12}\text{CO}$  is systematically greater than that for  $^{13}\text{CO}$  and  $\text{C}^{18}\text{O}$ , because the emission area of  $^{12}\text{CO}$  is systematically greater than that of  $^{13}\text{CO}$  and  $\text{C}^{18}\text{O}$ .

Yan et al. (2021) defined the sensitivity clip factor,  $\xi$ , as the ratio of the observed flux to the total flux. They also derived a relationship between the observed flux and the mean voxel S/N (defined as  $x$ ), and the ratio of the observed flux to the total flux is approximately given by  $(x - 2.224)^2 / (x - 2.224 + 0.457)^2$ . This relationship can be used to correct the total flux in our results.

Figure 8 shows the histogram distribution of the sensitivity clip factor for  $^{12}\text{CO}$ ,  $^{13}\text{CO}$ , and  $\text{C}^{18}\text{O}$  in the cloud catalog. It should be noted that unlike the mean voxel S/N for all the voxels in Yan et al. (2021), the mean voxel S/N of  $^{13}\text{CO}$  and  $\text{C}^{18}\text{O}$  in this paper is the mean of the S/N at the peak value within all pixels. This is because the mean voxel S/N of  $^{13}\text{CO}$  and  $\text{C}^{18}\text{O}$  is so low that the calculated S/N is smaller than 2.224, so we use the peak value to derive the clip factor. This results in  $\xi$  values being calculated for  $^{13}\text{CO}$  and  $\text{C}^{18}\text{O}$  that are generally higher than those for  $^{12}\text{CO}$ .

Figure 9 shows the relationships between the corrected flux based on the sensitivity clip factor  $\xi$  for  $^{12}\text{CO}$  and  $^{13}\text{CO}$  and for  $^{13}\text{CO}$  and  $\text{C}^{18}\text{O}$ , respectively. Figure 9 also presents a significant correlation between the fluxes of CO and its isotopic molecules, and the flux ratio values are consistent with those in Figure 5.

The corrected relationships between CO and its isotopic molecules' fluxes are  $F_{^{13}\text{CO}} = 0.15 F_{^{12}\text{CO}}$  and  $F_{\text{C}^{18}\text{O}} = 0.14 F_{^{13}\text{CO}}$ , respectively. The derived abundance of  $^{13}\text{CO}$  is  $5.7_{-0.4}^{+0.1} \times 10^{-7}$ , and the abundance ratio  $X_{^{13}\text{CO}}/X_{\text{C}^{18}\text{O}}$  is  $7.0_{-0.1}^{+1.1}$ .

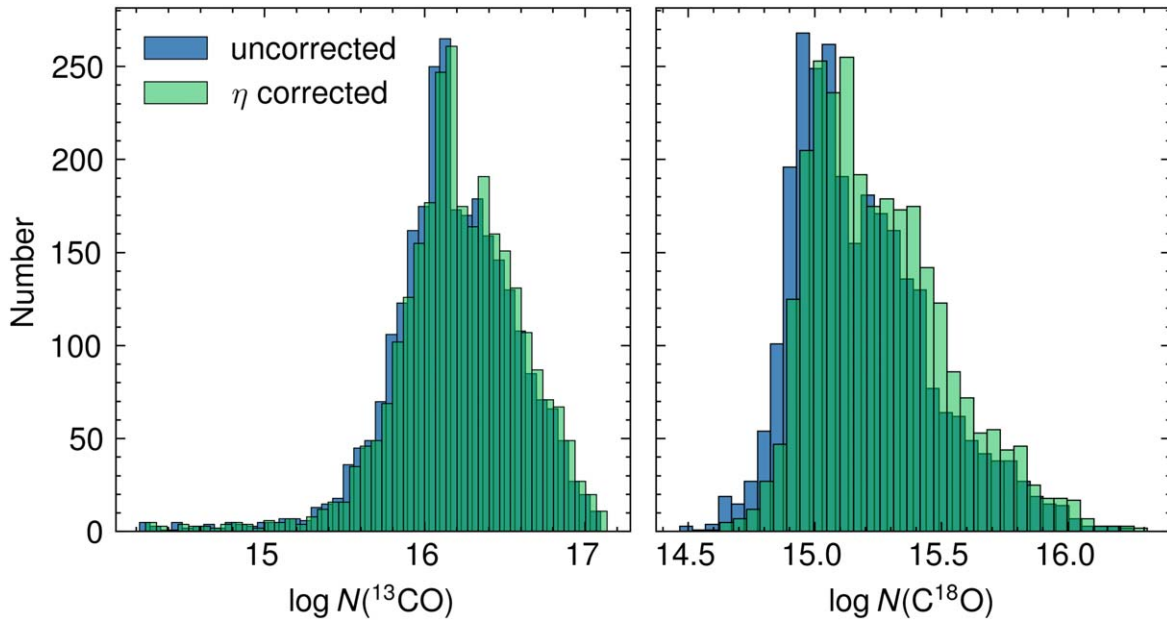
Figure 10 shows histogram distribution of the column density of  $^{13}\text{CO}$  and  $\text{C}^{18}\text{O}$  under the LTE assumption with or without the filling factor  $\eta$  being corrected. The  $\eta$ -corrected column density distribution is very close to the original column density distribution. This indicates that the column density is generally underestimated without correction for this factor, but the proportion of underestimation seems to be small.

Figure 11 presents the  $\eta$ -corrected  $N_{^{13}\text{CO}}$  versus  $X_{^{13}\text{CO}}/X_{\text{C}^{18}\text{O}}$  pixel by pixel measured in 32 clouds. Its overall distribution is consistent with Figure 7, but there are some more low-abundance points near the region where the  $^{13}\text{CO}$  column density is  $2 \times 10^{16} \text{ cm}^{-2}$ .

### 6.3. Abundance $X_{\text{C}^{18}\text{O}}$

The derived abundance  $X_{^{13}\text{CO}}$  and the  $X_{^{13}\text{CO}}/X_{\text{C}^{18}\text{O}}$  ratios of  $6.5_{-0.5}^{+0.1} \times 10^{-7}$  and  $9.7_{-0.8}^{+0.6}$ , respectively, suggest that the abundance of  $^{13}\text{CO}$  is higher compared to  $\text{C}^{18}\text{O}$ . Taking into account the sensitivity clip factor, the abundance of  $\text{C}^{18}\text{O}$  is corrected to be  $8.1_{-0.6}^{+0.3} \times 10^{-8}$ . This value is consistent with previous studies, such as Frerking et al. (1982), who determined  $X_{\text{C}^{18}\text{O}}$  for Taurus envelopes ( $7 \times 10^{-8}$ ) and dense cores ( $17 \times 10^{-8}$ ), based on  $^{12}\text{CO}$  ( $J = 1-0, 2-1$ ) and 1.3 mm continuum observations, and Hotzel et al. (2002), who derived  $X_{\text{C}^{18}\text{O}}$  between  $7 \times 10^{-8}$  (Coalsack) and  $20 \times 10^{-8}$  (Chamaeleon I). This indicates that the derived abundance of  $\text{C}^{18}\text{O}$  in this study is within the expected range, based on previous literature. As mentioned in Section 4, this conclusion is based on the LTE assumption and assuming that the MC has a relatively consistent optical thickness and excitation temperature. Moreover, as the correlated axes will induce a potential bias, we remain cautious about the result of a constant abundance  $X_{\text{C}^{18}\text{O}}$  over the sample.





**Figure 10.** Histogram distribution of the column density of  $^{13}\text{CO}$  and  $\text{C}^{18}\text{O}$  under the LTE assumption with or without the filling factor  $\eta$  being corrected.

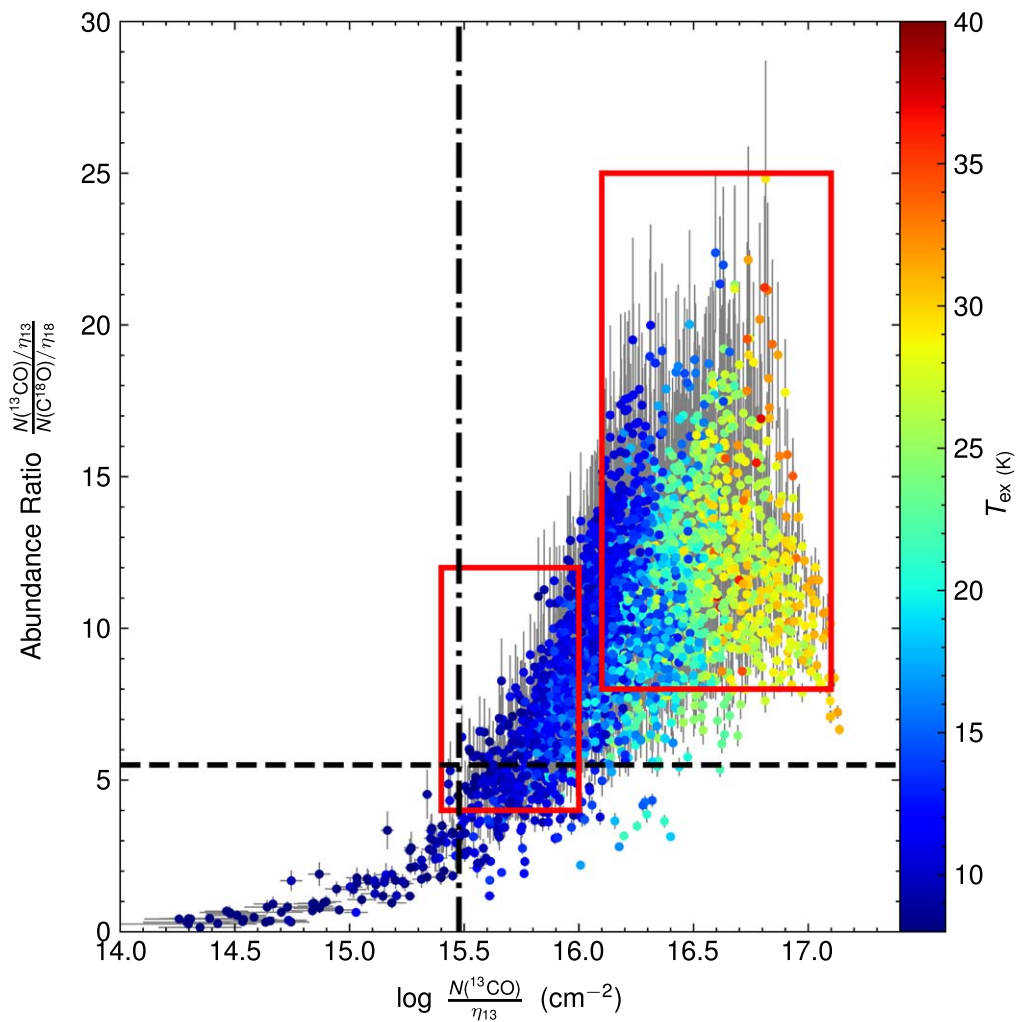


**Figure 11.**  $\eta$ -corrected  $N_{^{13}\text{CO}}$  vs.  $X_{^{13}\text{CO}}/X_{\text{C}^{18}\text{O}}$  pixel by pixel measured in 32 clouds. All the symbols and colors are same as in Figure 7, except the values of  $N_{^{13}\text{CO}}$  and  $X_{^{13}\text{CO}}/X_{\text{C}^{18}\text{O}}$  are corrected by the fill factor  $\eta$ .

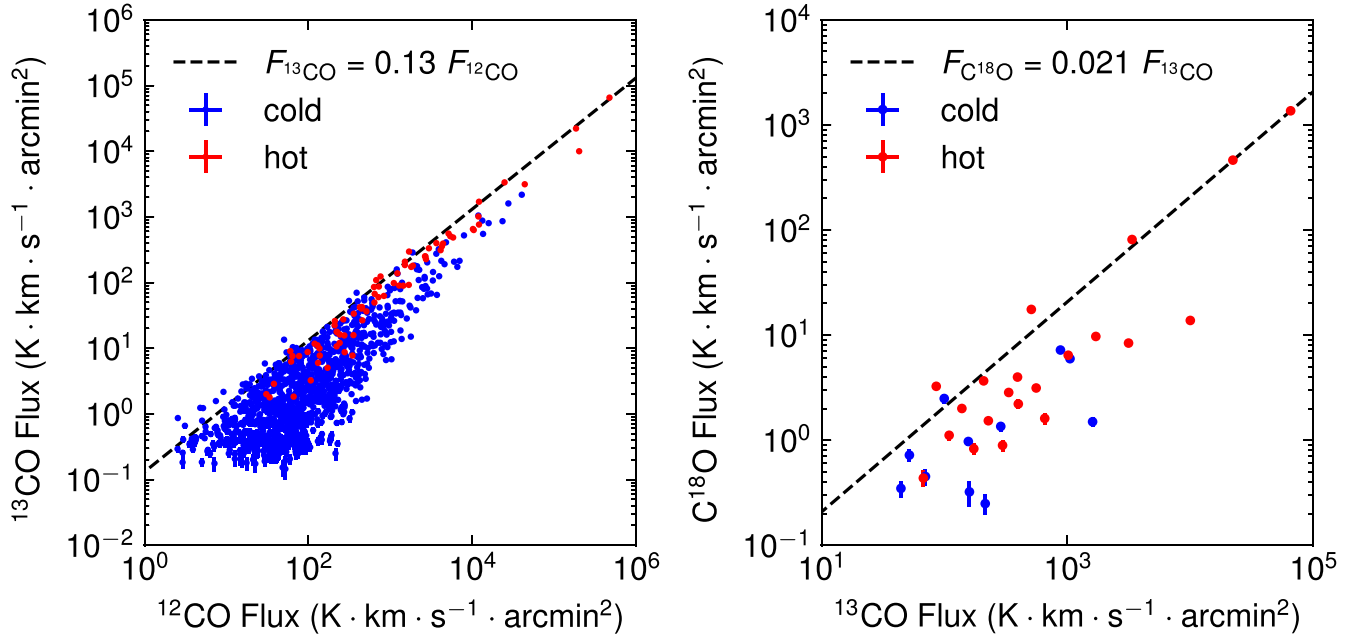


**Figure 12.** Left: flux ( $^{12}\text{CO}$ ) vs. flux ( $^{13}\text{CO}$ ) measured cloud by cloud in the 1197-cloud catalog. The flux ( $^{12}\text{CO}$ ) and flux ( $^{13}\text{CO}$ ) are calculated toward the entire cloud. Right: flux ( $^{13}\text{CO}$ ) vs. flux ( $\text{C}^{18}\text{O}$ ) measured in the 32-cloud catalog. The flux ( $^{13}\text{CO}$ ) and flux ( $\text{C}^{18}\text{O}$ ) are calculated toward the entire cloud. The colors indicate different types of MCs, based on excitation temperature. The dashed line shows the result of a weighted linear fit to the data.

#### 6.4. Flux

Figure 5 shows strong correlations between the flux of  $^{12}\text{CO}$  versus  $^{13}\text{CO}$  and  $^{13}\text{CO}$  versus  $\text{C}^{18}\text{O}$ , respectively. It should be noted that we kept the area the same for  $^{12}\text{CO}$  versus  $^{13}\text{CO}$  and  $^{13}\text{CO}$  versus  $\text{C}^{18}\text{O}$  when we calculated the flux. In fact, this linear relationship holds not only for the same areas where both CO and its isotopic emissions are detected, but also for the entire MC scale. Figure 12 shows the flux distributions of  $^{12}\text{CO}$  versus  $^{13}\text{CO}$  and  $^{13}\text{CO}$  versus  $\text{C}^{18}\text{O}$  calculated toward the entire cloud, respectively. Through flux-weighted linear fitting of the data, we get the relations  $F_{^{13}\text{CO}} = 0.13 F_{^{12}\text{CO}}$  and  $F_{\text{C}^{18}\text{O}} = 0.021 F_{^{13}\text{CO}}$ . The flux ratios of  $^{13}\text{CO}/^{12}\text{CO}$  and  $\text{C}^{18}\text{O}/^{13}\text{CO}$  calculated from entire MCs are slightly lower than those calculated from only the  $^{13}\text{CO}$ -bright and  $\text{C}^{18}\text{O}$ -bright regions, respectively, which was foreseeable, since the former calculation includes more extended areas than the latter. Although the ratios, i.e., the linear coefficients, in Figures 5 and 12 are different, the  $^{12}\text{CO}$  versus  $^{13}\text{CO}$  and  $^{13}\text{CO}$  versus  $\text{C}^{18}\text{O}$  emissions in the two figures exhibit obvious correlations. This may imply that the flux ratio has large-scale uniformity within the MC and that the flux ratios of these gases are close to the same proportions within each MC (e.g. Figure 13). It is worth noting that the dispersion of these points in Figure 12 increases significantly with the decrease of flux. This is most likely due to sensitivity limitations. On the other hand, as shown in Section 6.2, the beam filling factor is mainly correlated with the angular size. All of these can lead to the underestimation of the flux and cause a large distribution dispersion.

#### 6.5. LTE Assumption

As shown in Sections 1 and 3, it is a common method to use LTE assumptions to approximate temperature, opacity, and density. However, this method relies on assumptions that might not necessarily be met in our samples. Roueff et al. (2021) estimated the abundances, excitation temperatures, velocity

fields, and velocity dispersions of the three main CO isotopologues toward a subset of the Orion B MC, by using the CRB technique, and they found that excitation temperatures are different among  $^{12}\text{CO}$ ,  $^{13}\text{CO}$ , and  $\text{C}^{18}\text{O}$ :  $^{12}\text{CO}$  presents the highest temperature, followed by  $^{13}\text{CO}$  and  $\text{C}^{18}\text{O}$ . The ratios of the estimated temperatures among CO isotopologues are  $T_{\text{ex}}(^{12}\text{CO})/T_{\text{ex}}(^{13}\text{CO}) = 1.7$  and  $T_{\text{ex}}(^{13}\text{CO})/T_{\text{ex}}(\text{C}^{18}\text{O}) = 1.3$ . Padoan et al. (1997) obtain a theoretical calibration of the relation between the LTE  $^{13}\text{CO}$  column density and true column density by using models of MCs and non-LTE radiative transfer calculations. And they find that the LTE column density of MCs typically underestimates the mean  $^{13}\text{CO}$  true column density by a factor ranging from 1.3 to 7.

In this paper, we assume that CO and its isotopologues have the same excitation temperature, which may introduce some bias to the results. So we correct the excitation temperatures of  $^{13}\text{CO}$  and  $\text{C}^{18}\text{O}$  according to the modified formula  $T_{\text{ex}}(^{12}\text{CO})/T_{\text{ex}}(^{13}\text{CO}) = 1.7$  and  $T_{\text{ex}}(^{13}\text{CO})/T_{\text{ex}}(\text{C}^{18}\text{O}) = 1.3$  in the results of Roueff et al. (2021). After the correction, we find that about 40% of the  $^{13}\text{CO}$  spectra and 3.5% of the  $\text{C}^{18}\text{O}$  spectra have corrected excitation temperatures lower than their peak main-beam brightness temperatures, which implies that Equation (1) is invalid. This suggests that the modified formula for the excitation temperature may not hold true for all MCs. This may be because the Orion B MC (Roueff et al. 2021) studied has a more extreme environment relative to other MCs, which is not common in general MCs.

Figures 14 and 15 show the difference between the LTE column density and the column density after excitation temperature correction from  $^{13}\text{CO}$  and  $\text{C}^{18}\text{O}$  data. For the  $^{13}\text{CO}$  LTE column density before and after the correction, the ratio ranges from 25% to 150% and did not show any obvious trend with the temperature. For the  $\text{C}^{18}\text{O}$  LTE column density before and after the correction, the ratio tends to increase with higher  $T_{\text{ex}}$ . When  $T_{\text{ex}} > 15$  K, the  $\text{C}^{18}\text{O}$  LTE column density has a 150%–200% overestimate.

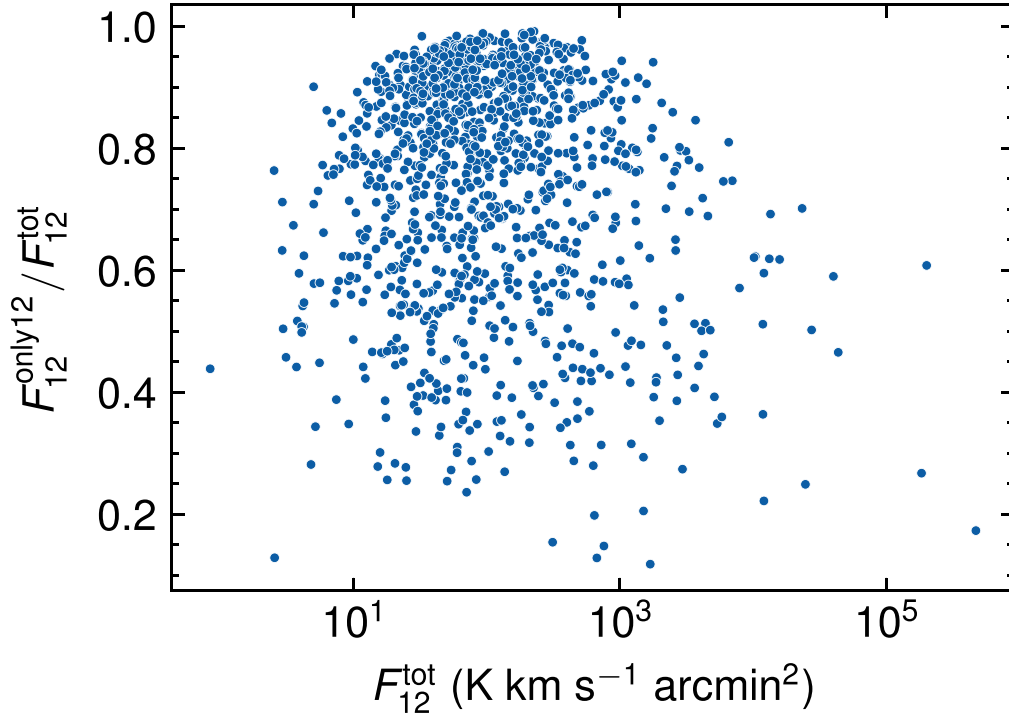


**Figure 13.**  $^{12}\text{CO}$  flux  $F_{12}^{\text{tot}}$  vs. flux proportion of the  $^{12}\text{CO}$ -only region in the 1197-cloud catalog.  $F_{12}^{\text{tot}}$  is calculated toward the entire cloud.

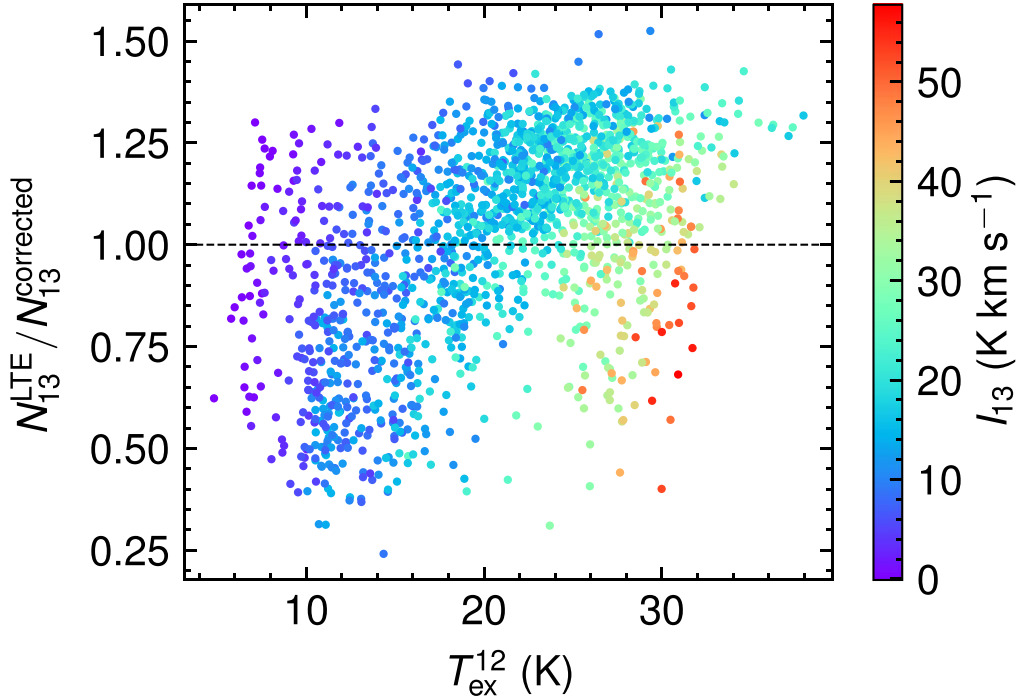


**Figure 14.** The ratio of  $N_{13}^{\text{LTE}}/N_{13}^{\text{corrected}}$  vs.  $T_{\text{ex}}^{12}$ .  $N_{13}^{\text{LTE}}$  is the  $^{13}\text{CO}$  column density under the LTE assumption, while  $N_{13}^{\text{corrected}}$  is the corrected  $^{13}\text{CO}$  column density, based on the corrected  $^{13}\text{CO}$  excitation temperature and the correlation  $T_{\text{ex}}(^{12}\text{CO})/T_{\text{ex}}(^{13}\text{CO}) = 1.7$ .  $T_{\text{ex}}^{12}$  is the excitation temperature from the  $^{12}\text{CO}$  spectrum under the LTE assumption. The color shows the intensity of  $^{13}\text{CO}$ .

Borchert et al. (2022) found that the intensity-weighted average excitation temperature results in the most accurate estimate of the total CO mass by simulation. Figure 16 shows the distribution of the intensity-weighted average excitation temperature in our samples. This suggests that most MCs have an overall temperature between 4 and 9 K.

## 7. Summary

In our study, we have analyzed data from the  $^{12}\text{CO}$ ,  $^{13}\text{CO}$ , and  $\text{C}^{18}\text{O}$  (1–0) transitions in a section of the third Galactic quadrant ( $195^\circ < l < 220^\circ$ ,  $|b| < 5^\circ$ ) within a velocity range of  $[-20, 70]$   $\text{km s}^{-1}$ , obtained from the MWISP CO survey, as described in Paper I. We have compared various observational

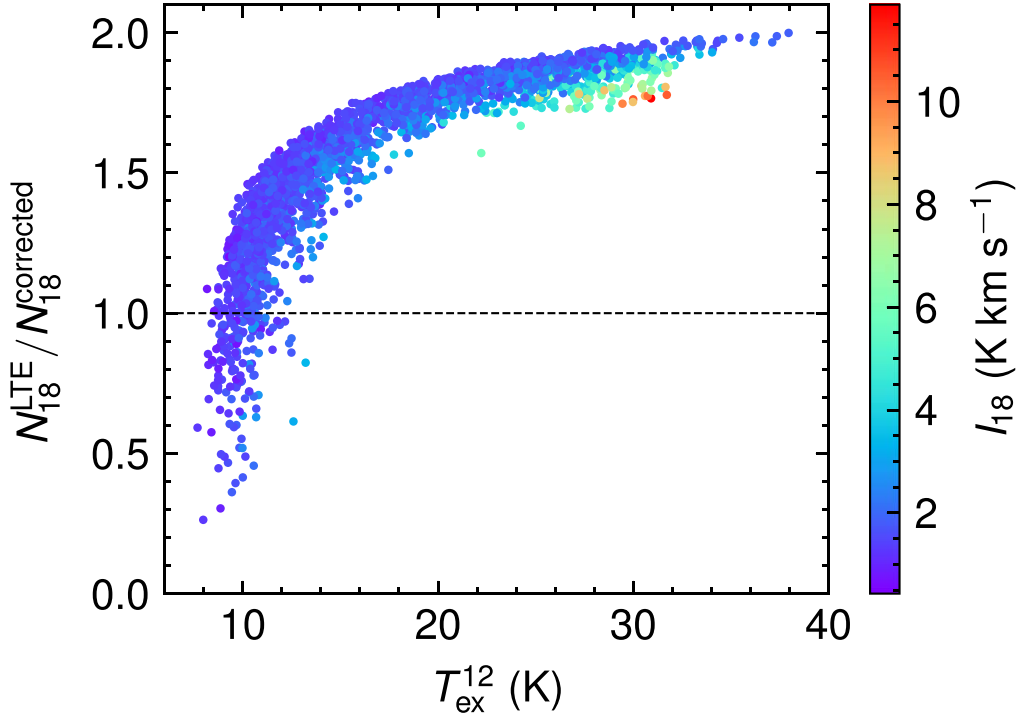


**Figure 15.** The ratio of  $N_{18}^{\text{LTE}}/N_{18}^{\text{corrected}}$  vs.  $T_{\text{ex}}^{12}$ .  $N_{18}^{\text{LTE}}$  is the  $^{18}\text{CO}$  column density under the LTE assumption, while  $N_{18}^{\text{corrected}}$  is the corrected  $^{18}\text{CO}$  column density based on the corrected  $^{18}\text{CO}$  excitation temperature and correlation  $T_{\text{ex}}(^{13}\text{CO})/T_{\text{ex}}(\text{C}^{18}\text{O}) = 1.3$ .  $T_{\text{ex}}^{12}$  is the excitation temperature from the  $^{12}\text{CO}$  spectrum under the LTE assumption. The color shows the intensity of  $^{18}\text{CO}$ .

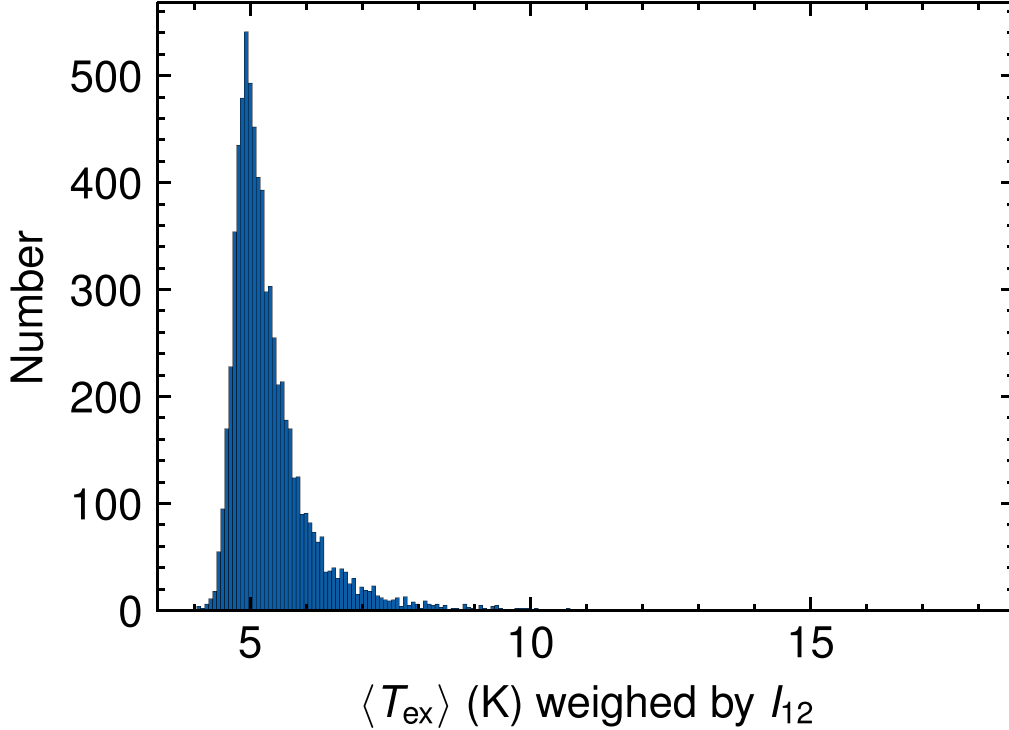


**Figure 16.** The histogram of the intensity-weighted average excitation temperatures from  $^{12}\text{CO}$  data.

properties among the three isotopologues and summarized their parameter space based on cloud samples identified in Paper I. Our analysis has revealed some new findings, and we have observed that although the parameters have a wide distribution, they tend to concentrate in certain intervals, according to the probability density functions of the pixels:

1. The peak intensities of  $^{12}\text{CO}$ ,  $^{13}\text{CO}$ , and  $\text{C}^{18}\text{O}$  are mainly concentrated in the range of [3, 8], [1.5, 4], and [0.7, 1.5] K, respectively, with mean values of 6.9, 2.0, and 1.3 K, respectively.
2. The optical depths of  $^{12}\text{CO}$ ,  $^{13}\text{CO}$ , and  $\text{C}^{18}\text{O}$  are primarily distributed in the interval of [15, 40], [0.2, 0.4], and [0.05,



0.15], respectively, with mean values of 32, 0.36, and 0.12, respectively.

3. The integrated intensities of  $^{12}\text{CO}$ ,  $^{13}\text{CO}$ , and  $\text{C}^{18}\text{O}$  are concentrated in the range of [5, 25], [0.4, 5], and [0.6, 2.5]  $\text{K km s}^{-1}$ , respectively. The majority of pixels have a ratio of  $I^{13\text{CO}}/I^{12\text{CO}}$  in the range of [0.1, 0.2] and a  $I^{\text{C}^{18}\text{O}}/I^{13\text{CO}}$  ratio value of approximately 0.1.

4. The angular area  $A^{13\text{CO}}$  of  $^{13}\text{CO}$  increases with  $A^{12\text{CO}}$  and its dispersion decreases. The ratio  $A^{13\text{CO}}/A^{12\text{CO}}$  is 0.38 by linear fitting.

The relationship between CO and its isotope molecules' flux in MCs has been found to exhibit significant correlations. The first relationship is between the  $^{12}\text{CO}$  and  $^{13}\text{CO}$  flux, which shows a correlation of  $F^{13\text{CO}} = 0.17 F^{12\text{CO}}$  across a wide range of fluxes spanning six orders of magnitude, cloud by cloud. This indicates that the abundance  $X^{13\text{CO}}$  is a constant for the entire sample and the X-factor, which is the ratio of the CO column density to its integrated intensity, is ubiquitous in a large sample of MCs and maintains a stable value. The derived abundance of  $^{13}\text{CO}$ , denoted as  $X^{13\text{CO}}$ , is determined to be  $6.5_{-0.5}^{+0.1} \times 10^{-7}$  under the LTE assumption, which remains the same across the MC as a whole.

The second significant correlation is found between the  $^{13}\text{CO}$  and  $\text{C}^{18}\text{O}$  flux, expressed as  $F^{\text{C}^{18}\text{O}} = 0.11 F^{13\text{CO}}$ , cloud by cloud. This indicates that the abundance ratio  $X^{13\text{CO}}/X^{\text{C}^{18}\text{O}}$  remains at the same value of  $9.7_{-0.8}^{+0.6}$  across the MC as a whole under the LTE assumption. The derived abundance of  $\text{C}^{18}\text{O}$ , denoted as  $X^{\text{C}^{18}\text{O}}$ , is determined to be  $6.7_{-0.9}^{+0.7} \times 10^{-8}$ .

The linear relationships of  $F^{12\text{CO}}$  versus  $F^{13\text{CO}}$  and  $F^{13\text{CO}}$  versus  $F^{\text{C}^{18}\text{O}}$  hold not only for the  $^{13}\text{CO}$ -bright region and the  $\text{C}^{18}\text{O}$ -bright region, but also for the entire MC scale with a lower flux ratio.

After considering the observation uncertainties, the corrected relationships between CO and its isotope molecules' flux are found to be  $F^{13\text{CO}} = 0.15 F^{12\text{CO}}$  and  $F^{\text{C}^{18}\text{O}} = 0.14 F^{13\text{CO}}$ , respectively. This leads to a derived abundance of  $X^{13\text{CO}}$  as  $5.7_{-0.4}^{+0.1} \times 10^{-7}$  and an abundance ratio of  $X^{13\text{CO}}/X^{\text{C}^{18}\text{O}}$  as  $7.0_{-0.1}^{+0.1}$ . The abundance of  $X^{\text{C}^{18}\text{O}}$  is determined to be  $8.1_{-0.6}^{+0.3} \times 10^{-8}$ .










The abundance ratio  $X^{13\text{CO}}/X^{\text{C}^{18}\text{O}}$  shows a strong correlation with column density and temperature. The value of  $X^{13\text{CO}}/X^{\text{C}^{18}\text{O}}$  is generally higher than the terrestrial ratio of 5.5, indicating that chemical fractionation, selective dissociation, and self-shielding effects play an important role in determining the isotopic abundance ratios in MCs. Although local environmental differences may cause some variation in  $X^{13\text{CO}}$  and  $X^{13\text{CO}}/X^{\text{C}^{18}\text{O}}$  within the MC, on a global scale, they both maintain a stable value cloud by cloud and are independent of evolution. This implies that while local properties of MCs may be affected by star-forming activities during the evolutionary process, such as changes in temperature, density, and abundance, the overall properties of MCs do not change significantly.

### Acknowledgments

This research has made use of data from the Milky Way Imaging Scroll Painting (MWISP) project, which is a multiline survey in  $^{12}\text{CO}/^{13}\text{CO}/\text{C}^{18}\text{O}$  along the northern galactic plane with the PMO 13.7 m telescope. We are grateful to all the members of the MWISP working group, particularly the staff members at the PMO 13.7 m telescope, for their long-term

support. MWISP was sponsored by the National Key R&D Program of China with grant 2017YFA0402701 and the CAS Key Research Program of Frontier Sciences with grant QYZDJ-SSW-SLH047. This work is supported by the Natural Science Foundation of Jiangsu Province (grant No. BK20201108). This work is supported by the National Natural Science Foundation of China (grant No. 12073079). J.Y. is supported by the National Natural Science Foundation of China through grant 12041305. C.W. is thankful for the support from the China Postdoctoral Science Foundation (No. 2022M713173). Y.S. is supported by the National Natural Science Foundation of China (grant No. 12173090). We are also thankful for the support from the Millimeter Wave Radio Astronomy Database (<http://www.radioast.csdb.cn/>). C.W. is grateful for the funding as a FAST Fellow. We would like to thank the referee for going through the paper carefully and much appreciate the many constructive comments that improved it.

### ORCID iDs

Chen Wang  <https://orcid.org/0000-0001-8923-7757>  
 Haoran Feng  <https://orcid.org/0000-0003-1714-0600>  
 Ji Yang  <https://orcid.org/0000-0001-7768-7320>  
 Xuepeng Chen  <https://orcid.org/0000-0003-3151-8964>  
 Yang Su  <https://orcid.org/0000-0002-0197-470X>  
 Qing-Zeng Yan  <https://orcid.org/0000-0003-4586-7751>  
 Fujun Du  <https://orcid.org/0000-0002-7489-0179>  
 Yuehui Ma  <https://orcid.org/0000-0002-8051-5228>  
 Jiajun Cai  <https://orcid.org/0000-0002-9649-8549>

### References

- Bolato, A. D., Wolfire, M., & Leroy, A. K. 2013, *ARA&A*, 51, 207  
 Borchert, E. M. A., Walch, S., Seifried, D., et al. 2022, *MNRAS*, 510, 753  
 Bourke, T. L., Garay, G., Lehtinen, K. K., et al. 1997, *ApJ*, 476, 781  
 Dame, T. M., Hartmann, D., & Thaddeus, P. 2001, *ApJ*, 547, 792  
 Frerking, M. A., Langer, W. D., & Wilson, R. W. 1982, *ApJ*, 262, 590  
 Garden, R. P., Hayashi, M., Hasegawa, T., Gatley, I., & Kaifu, N. 1991, *ApJ*, 374, 540  
 Herwig, F., & Austin, S. M. 2004, *ApJL*, 613, L73  
 Hollenbach, D. J., & Tielens, A. G. G. M. 1997, *ARA&A*, 35, 179  
 Hotzel, S., Harju, J., Juvela, M., Mattila, K., & Haikala, L. K. 2002, *A&A*, 391, 275  
 Kong, S., Lada, C. J., Lada, E. A., et al. 2015, *ApJ*, 805, 58  
 Lang, K. R. 1980, *Astrophysical Formulae. A Compendium for the Physicist and Astrophysicist* (Berlin: Springer)  
 Langer, W. D., Graedel, T. E., Frerking, M. A., & Armentrout, P. B. 1984, *ApJ*, 277, 581  
 Liszt, H. S. 2007, *A&A*, 476, 291  
 Loison, J.-C., Wakelam, V., Gratier, P., et al. 2019, *MNRAS*, 485, 5777  
 Lyons, J. R., & Young, E. D. 2005, *Natur*, 435, 317  
 Ma, Y., Wang, H., Zhang, M., et al. 2022, *ApJS*, 262, 16  
 Milam, S. N., Savage, C., Brewster, M. A., Ziurys, L. M., & Wyckoff, S. 2005, *ApJ*, 634, 1126  
 Nagahama, T., Mizuno, A., Ogawa, H., & Fukui, Y. 1998, *AJ*, 116, 336  
 Padoan, P., Juvela, M., Bally, J., & Nordlund, A. 1997, arXiv:astro-ph/9706177  
 Pagel, B. E. J. 1997, *Nucleosynthesis and Chemical Evolution of Galaxies* (Cambridge: Cambridge Univ. Press)  
 Pineda, J. E., Caselli, P., & Goodman, A. A. 2008, *ApJ*, 679, 481  
 Pineda, J. L., Goldsmith, P. F., Chapman, N., et al. 2010, *ApJ*, 721, 686  
 Rohlfs, K., & Wilson, T. L. 2000, *Obs*, 120, 289  
 Romano, D., Matteucci, F., Zhang, Z. Y., Papadopoulos, P. P., & Ivison, R. J. 2017, *MNRAS*, 470, 401  
 Roueff, A., Gerin, M., Gratier, P., et al. 2021, *A&A*, 645, A26  
 Shan, W., Yang, J., Shi, S., et al. 2012, *ITST*, 2, 593  
 Shimajiri, Y., Kitamura, Y., Nakamura, F., et al. 2015, *ApJS*, 217, 7  
 Shimajiri, Y., Kitamura, Y., Saito, M., et al. 2014, *A&A*, 564, A68  
 Sliwa, K., Wilson, C. D., Aalto, S., & Privon, G. C. 2017, *ApJL*, 840, L11

- Smith, R. L., Pontoppidan, K. M., Young, E. D., Morris, M. R., & van Dishoeck, E. F. 2009, [ApJ](#), **701**, 163
- Sun, Y., Yang, J., Xu, Y., et al. 2020, [ApJS](#), **246**, 7
- Szűcs, L., Glover, S. C. O., & Klessen, R. S. 2014, [MNRAS](#), **445**, 4055
- Timmes, F. X., Woosley, S. E., & Weaver, T. A. 1995, [ApJS](#), **98**, 617
- van Dishoeck, E. F., & Black, J. H. 1988, [ApJ](#), **334**, 771
- Visser, R., van Dishoeck, E. F., & Black, J. H. 2009, [A&A](#), **503**, 323
- Wang, C., Feng, H., Yang, J., et al. 2023, [AJ](#), **165**, 106
- Wang, C., Yang, J., Su, Y., et al. 2019, [ApJS](#), **243**, 25
- Warin, S., Benayoun, J. J., & Viala, Y. P. 1996, [A&A](#), **308**, 535
- Watson, W. D., Anicich, V. G., & Huntress, W. T., Jr. 1976, [ApJL](#), **205**, L165
- Wilson, T. L., & Matteucci, F. 1992, [A&ARv](#), **4**, 1
- Wilson, T. L., Rohlf, K., & Hüttemeister, S. 2009, *Tools of Radio Astronomy* (Berlin: Springer)
- Wu, Y., Liu, T., Meng, F., et al. 2012, [ApJ](#), **756**, 76
- Yan, Q.-Z., Yang, J., Yang, S., Sun, Y., & Wang, C. 2021, [ApJ](#), **910**, 109
- Yang, J., Shan, W., Shi, S., et al. 2008, in *2008 Global Symp. on Millimeter Waves* (New York: IEEE), 177
- Yuan, L., Yang, J., Du, F., et al. 2022, [ApJS](#), **261**, 37